



HAL
open science

Bioelectric signaling and the control of cardiac cell identity in response to mechanical forces

Hajime Fukui, Renee Wei-Yan Chow, Jing Xie, Yoke Yin Foo, Choon Hwai Yap, Nicolas Minc, Naoki Mochizuki, Julien Vermot

► **To cite this version:**

Hajime Fukui, Renee Wei-Yan Chow, Jing Xie, Yoke Yin Foo, Choon Hwai Yap, et al.. Bioelectric signaling and the control of cardiac cell identity in response to mechanical forces. *Science*, 2021, 374 (6565), pp.351-354. 10.1126/science.abc6229 . hal-03821110

HAL Id: hal-03821110

<https://hal.science/hal-03821110v1>

Submitted on 19 Oct 2022

HAL is a multi-disciplinary open access archive for the deposit and dissemination of scientific research documents, whether they are published or not. The documents may come from teaching and research institutions in France or abroad, or from public or private research centers.

L'archive ouverte pluridisciplinaire **HAL**, est destinée au dépôt et à la diffusion de documents scientifiques de niveau recherche, publiés ou non, émanant des établissements d'enseignement et de recherche français ou étrangers, des laboratoires publics ou privés.

1 **Molecular control of endocardial cell fate in response to mechanical forces during**
2 **cardiac valve formation**

3

4

5

6 Hajime Fukui^{1,2}, Renee Wei-Yan Chow¹, Jing Xie³, Vivek Vasudevan⁴, Choon Hwai
7 Yap^{4,5}, Nicolas Minc³, Naoki Mochizuki² and Julien Vermot^{1,5}

8

9 ¹ Institut de Génétique et de Biologie Moléculaire et Cellulaire (IGBMC), Centre National
10 de la Recherche Scientifique UMR7104, Institut National de la Santé et de la Recherche
11 Médicale U1258 and Université de Strasbourg, Illkirch, France

12 ² Department of Cell Biology, National Cerebral and Cardiovascular Center Research
13 Institute, Suita, Japan

14 ³ Université de Paris, Centre National de la Recherche Scientifique UMR7592, Institut
15 Jacques Monod, Paris, France

16 ⁴ Department of Biomedical Engineering, National University of Singapore, Singapore,
17 Singapore

18 ⁵ Department of Bioengineering, Imperial College London, London, United Kingdom

19

20 **Abstract**

21 Developing cardiovascular systems use mechanical forces at all organizational scales to
22 shape tissue. How ubiquitous blood flow forces instruct local cardiac cell identity is still
23 unclear. By manipulating mechanical forces *in vivo*, we show that ectopic shear stress is
24 necessary and sufficient to promote ectopic valve like structure **by activating cellular**
25 **valve identity and Endothelial to Mesenchymal Transition**. We found ectopic valve
26 formation results from the activation of two mechanosensitive pathways acting in parallel,
27 the well-established TRP-klf2a-wnt9b axis and an extracellular ATP-dependent
28 purinergic receptor pathway specifically triggering Ca²⁺ oscillation and Nfatc1
29 activation. Thus, mechanical forces are converted into discrete bioelectric signals by
30 synergistic mechanosensitive pathways to generate positional information and control
31 valve formation.

32

33

34

35 **Main Text:**

36 The cardiovascular system is continuously exposed to mechanical forces, such as fluid
37 shear stresses and stretching forces generated by blood flow and heartbeat. The
38 mechanotransduction cascade translates forces into cellular biochemical signals in the
39 cell (1, 2). The lumen of the cardiovascular system is lined by endocardial cells (EdCs)
40 and endothelial cells (ECs). These cell types present unique functional properties and
41 differentially respond to forces depending on the type of blood vessels or heart regions
42 they belong to (3-6). Heart valve defects are common human congenital anomalies, with
43 an incidence close to 2% of live births (7). While a number of valvular heart defects have
44 been linked to specific genetic mutations (e.g.,
45 in *NOTCH1*, *TBX5*, *GATA4*, *TBX20*, *LMCD1*, *TNS1*, and *DCHS1*) (8-12), the majority
46 have no clear environmental or genetical cause (13). Thus, it is thought that non
47 genetically encoded factors play an essential role in the genesis of congenital valve
48 defects. The forces generated in the heart are significantly higher than in the vascular
49 system where pathologies related to mechanical forces start to be well established (14,
50 15). Consequently, the molecular mechanisms underlying force sensitivity of endothelial
51 cells in the heart (i.e. EdCs) are likely to be different from vascular endothelial cells and
52 remain largely unknown. Calcium ion (Ca^{2+}) signaling is often associated with the direct
53 cellular response to mechanical forces and initiates the mechanosensitive response in
54 endothelial cells (16). Yet, how Ca^{2+} signaling leads to a cell specific response to
55 mechanical forces remains unclear. Here, we examine the ability of mechanical forces to
56 modulate specific endocardial fate towards valvulogenesis. We directly tested the
57 signaling cascades activated by mechanical forces, quantitatively characterized their
58 dynamic properties, and considered the implications of these observations for

59 transcriptional regulation of valve-specific markers *in vivo*. We find that valvular cell
60 identity is directed by blood flow via two different mechanosensitive pathways: TRP
61 mediated *klf2a* activation and ATP mediated Ca²⁺ oscillation leading to Nfatc1 signaling
62 in response to local high shear stresses.

63

64 Using the zebrafish model system to allow for high precision control of spatiotemporal
65 mechanical parameters (17, 18), we analyzed Ca²⁺ dynamic patterns via **live imaging of**
66 **the endocardium at cellular resolution**. Ca²⁺ fluctuations are observed in many
67 developmental contexts associated with tissue reorganization such as cell migration (19),
68 wound healing (20), embryonic development, and regeneration (21, 22). In endothelial
69 cells, Ca²⁺ fluxes have been shown to be involved in angiogenesis (23, 24). Thus, it is
70 thought that Ca²⁺ is an important effector of cardiovascular morphogenesis. To address
71 whether Ca²⁺ activation can be observed specifically in the EdCs, we expressed the
72 fluorescent Ca²⁺ sensor protein GCaMP7a in endocardial/endothelial cells using a
73 *Tg(fli1a:gal4ff);(uas:GCaMP7a)* system (24) along with *Tg(kdrl:nls-mCherry)*. We
74 found that Ca²⁺ oscillations were observed almost exclusively in the EdCs of the
75 atrioventricular canal (AVC) (Fig. 1, A to D, **Fig. S1A** and Movie S1) between 32 and
76 **102** hpf (hours post fertilization). Normalization of the calcium signal obtained by
77 computing the ratiometric intensity of GCaMP7a to nls-mCherry signals in tracked EdCs
78 confirms that EdCs display Ca²⁺ oscillations (Fig. 1B and Movie S2). The occurrence of
79 Ca²⁺ oscillations peaks at around 2.5 dpf and subsequently declines as the morphogenesis
80 of functional valves proceeds (Fig. 1C). We found that around two thirds of EdCs in the
81 AVC display Ca²⁺ oscillating at 54 hpf, and that this number decreases at later
82 developmental stages (Fig. **S1B**). Similarly, the oscillation frequency reaches a maximum

83 at 54 hpf and declines at later stages (Fig. S1C). Interestingly, we found that the period
84 of Ca²⁺ activation does not significantly vary with development stages even when the
85 overall activity declines (Fig. S1D).

86

87 To verify that the calcium oscillations are associated with valvulogenic differentiation,
88 we next searched for the decoder/effector of this Ca²⁺ signaling. Nuclear factor of
89 activated T-cells (Nfatc1) is an established Ca²⁺ sensitive transcription factor known to
90 control EndoMT and subsequent heart valve morphogenesis (25-30). The inactive form
91 of Nfat is phosphorylated and sequestered in the cytoplasm. Nfatc1 activation is mediated
92 by calcium via the calmodulin dependent serine/threonine protein phosphatase
93 Calcineurin in response to Ca²⁺ (43). Upon the activation of Calcineurin, Nfat is de-
94 phosphorylated and subsequently translocated to the nucleus to activate transcription (30,
95 31). Nfatc1 is thus both a good marker of valve cell identity and a candidate for a relay
96 protein decoding the levels of cytoplasmic Ca²⁺ to generate a transcriptional response.
97 (Fig. S2A). We generated a Nfat binding element reporter line, *Tg(4xnfbr:d2EGFP)*,
98 which expresses d2EGFP in response to the binding of nuclear-localized Nfat protein (Fig.
99 S2B). Nfat reporter expression was observed in EdCs of the AVC from 34 hpf onward
100 (Fig. 1, E and F, and Fig. S2C). At 78 hpf, the number of d2EGFP positive cells starts to
101 decrease in the EdCs of AVC, but the reporter still displays a specific expression in EdCs
102 in the AVC (Fig. 1E). Nfat reporter activation was thus strikingly similar to the time
103 course observed for the Ca²⁺ response (Fig. 1, C and F). To confirm these results, we
104 additionally tracked Nfat nuclear re-localization by generating an
105 endothelial/endocardial-specific GFP-Nfatc1 reporter allowing to monitor Nfat
106 subcellular distribution (Fig. S2F). As expected, we found that the GFP-Nfatc1

107 localisation varies in the endocardium with strong nuclear localization in the AVC while
108 GFP-Nfatc1 remains cytoplasmic in the other cells of the endocardium (Fig. S2F).

109 Together, these results highlight that both spatial and temporal regulation of Ca²⁺
110 signaling and Nfat activation are unique features of the EdCs located in the developing
111 valve area during heart development, suggesting an important role during valve formation
112 in response to mechanical forces.

113

114 Previous studies have shown that Ca²⁺ levels in EdCs are associated with changes in
115 mechanical forces but Ca²⁺ dynamics in response to mechanical force changes have never
116 been described (4). To test if the observed Ca²⁺ oscillations in EdCs are force-responsive,
117 we first assessed the Ca²⁺ signals in hearts stopped using of MS-222 or p-amino
118 blebbistatin treatment. We found that in these conditions, Ca²⁺ activation was abrogated
119 in EdCs (Fig. S3, A to C). Importantly, Ca²⁺ oscillations recovered upon wash-out and
120 restarting of the heartbeat (Fig. S3, A and B). Next, we assessed the impact of decreased
121 flow forces associated with lower hematocrit by analyzing the *gatala* mutant zebrafish
122 line that do not have red blood cells (32-34). Lower hematocrit significantly affects shear
123 stress and flow profile in the AVC (35, 36). Consistent with the heart-arrested condition,
124 *gatala* mutants (and *gatala* morphants), exhibited a decreased number of Ca²⁺ spikes at
125 both 54 hpf and 76 hpf (Fig. S3, D and E). We also found a significant decrease of Nfat
126 activity in the *gatala* mutants (Fig. S3F). Together, these results suggest that both Ca²⁺
127 oscillations and Nfat activation are stimulated in response to mechanical forces generated
128 by the beating heart.

129

130 In the heart, cardiomyocytes have been proposed to activate EdC responses to forces,

131 suggesting that endocardial cells are not the direct force sensor (37). It is thus important
132 to confirm that mechanical forces are indeed directly leading to Ca^{2+} signaling in the
133 endocardium. Consequently, we set out to alter the mechanical force distribution in the
134 living heart by artificially changing the boundary conditions and thus the flow forces in
135 the system (Fig. 2A). To this end, we inserted single agarose-based magnetic beads into
136 the cardiac lumen by microsurgery using 30-60 μm diameter beads that can be inserted
137 in the atrium or the ventricle without completely blocking heart function and flow in the
138 beating heart (Fig. 2B and Movie S3). The presence of the bead in the heart alters the
139 flow forces generated in the beating heart. To quantify the flow generated around the bead,
140 we performed a 3D simulation of the wall shear stress and pressure around the bead using
141 image-based computational fluid dynamics simulation **with a dynamic wall motion** (38)
142 (Fig. 2C and Fig. S4, A to C). We found that both parameters are increased in the vicinity
143 of the bead, indicating an increase in the flow forces generated around the grafted bead
144 (Movie S4). Interestingly, the calculated wall shear stress amplitude generated by the
145 presence of the bead in the atrium (3 Pa) is close to the endogenous wall shear stress
146 amplitude generated in the AVC at 48 hpf where the valve normally forms (between 3
147 and 7 Pa) (4, 38, 39). *In vivo*, we analysed the Ca^{2+} response of the EdCs and found that
148 Ca^{2+} spikes were observed in the EdCs close to the bead when trapped in the atrium or in
149 the ventricle, whereas sham injected embryos never display any Ca^{2+} activation except in
150 the AVC (Fig. 2D, Fig. S4, D and E, and Movie S5 and S6). The Ca^{2+} activation period
151 lasted an average of 5.5 sec around beads in the EdCs of the atrium or the ventricle (Fig.
152 S4F).

153

154 To further demonstrate that the impact of shear stress directly affects the EdC calcium

155 response in live embryo, we directly manipulated the bead within the heart using magnetic
156 tweezers. This approach permits to generate controlled shear forces in an immobilized
157 heart (Fig. 2E). We first calibrated the velocity of the bead pulled by the magnetic tweezer
158 and quantified the amount of force it can generate in the zebrafish heart (Fig. S4, G and
159 H). We found that the force generated by the magnetic bead in motion ranged between
160 100 to 2000 pN, a stimulus which is slightly higher than endogenous wall shear stresses
161 generated in the AVC (4, 38, 39). While the magnet probe alone did not affect Ca²⁺ influx
162 in EdCs, direct pulling of the magnetic bead lead to the generation of Ca²⁺ influx in the
163 EdCs of the arrested heart (Fig. 2, F to H, Fig. S4, I and J, and Movie S7). Together, these
164 results indicate that Ca²⁺ fluxes are induced in the EdCs by mechanical forces such as
165 wall shear stress and associated wall pressure.

166

167 We next assessed the biological relevance of the localized response initiated by bead
168 grafting and tested the role of ectopic forces in the initiation of valve formation.
169 Considering that bead grafting leads to the generation of a typical mechanosensitive
170 response in ectopic areas of the heart, we addressed if it is associated with the formation
171 of ectopic valves. Notably, 16-20 hours after bead grafting in the atrium, valve-like EdCs
172 clusters were observed near the grafted beads. The valve like structures were visible in
173 the atrial region that protruded from the atrial surface to the atrial cavity or the cardiac
174 jelly, respectively (Fig. 3A). We found that both the activity of Nfat and Notch signaling,
175 which are specific to valve cell identity (40-42), were strongly activated in the valve like
176 EdCs cluster generated near the grafted bead (Fig. 3A and Fig. S5A). To confirm the
177 results, we grafted a bead into atrial lumen at 50 hpf or 74 hpf and assessed the Nfat
178 reporter activity as a response to increase forces. Four hours after bead grafting, Nfat

179 reporter response was ectopically activated in EdCs located near the bead (Fig. 3B and
180 Fig. S5B). These results were consistent with the fact that Nfat activity is dramatically
181 reduced when heart contractility is affected (Fig. S5, C and D). Conversely, we found that
182 Nfatc1 nuclear localization is activated in response to ectopic forces (Fig. S5E). We could
183 confirm that nuclear activity of nfatc1 is dependent on the ser/thr de-phosphorylation by
184 using a chemical blocker of Calcineurin (FK506) (Fig. S5E). Thus, the nuclear
185 localization of GFP-Nfatc1 is promoted by increased mechanical force, in a Nfatc1 ser/thr
186 de-phosphorylation dependent manner.

187

188 To clarify the cell identities within the ectopic structures, we followed two different
189 approaches. We first generated a BAC transgenic line using the well-established EndoMT
190 marker *twist1b*, *TgBAC(twist1b:GFP)*, to highlight cells that underwent EndoMT in the
191 valvuloids. We clearly found Twist1b positive cells undergoing EndoMT in the
192 developing valve cushion and strong expression in the mesenchymal cells of the
193 developing valve (Fig. S6, A to C). When ectopic forces generated by beads lead to
194 valvuloid structures, Twist1b positive cells were populating the valve-like structure (Fig.
195 3C). We also observed that the grafted beads trigger the generation of mis-localised
196 protrusions into cardiac jelly, which constitute the first sign of cardiac valve
197 morphogenesis in zebrafish (44) (Fig. 3A). This observation along with the presence of
198 Nfat and Notch positive cells indicate that the ectopic valve like structures have important
199 similarities with endogenous valves.

200

201 To further confirm these observations, we next assessed if other valve related genes are
202 induced in response to the presence of ectopic forces in the endocardial cells (Fig. S6, D

203 to H). *Klf2* and *Wnt9b* have been shown to control heart valve remodeling in response to
204 mechanical forces in mouse and zebrafish (45). Using RNAscope, we found that the
205 grafted beads induced the ectopic expression of *klf2a* and *wnt9b* in the endocardial cells
206 surrounding it. In addition, we found that *klf4a*, a known modulator of EndoMT in EC
207 (46, 47) was also activated in response to ectopic forces. Interestingly, both *klf2a* and
208 *klf4a* expression were not affected when calcineurin was inhibited FK506, suggesting that
209 Ca^{2+} -Nfat signaling pathway act independently of the *klf2a-wnt9b* mechano-transduction
210 pathway. Conversely, *egr1*, a known mechanosensitive gene specifically expressed in the
211 AVC (48), was downregulated by calcineurin inhibition (Fig. S6, I and J). This suggests
212 that *egr1* acts downstream of Nfatc1. Thus, endocardial cells experiencing ectopic forces
213 activate the morphogenetic program which is promoting the expression of valve
214 remodeling and EndoMT markers required for the endogenous AV valve development.
215 These results demonstrate that mechanical forces are key to specify heart valve position
216 during development by modulating both the *Klf2a-Wnt9b* and the Nfatc1 signaling
217 pathways.

218

219 Considering Nfat and *Klf2a-Wnt9b* seem to define two different mechanosensitive
220 pathways, we next characterized the factors which are responsible for the force-dependent
221 Ca^{2+} - Nfat signal activation. We first focused on stretch sensitive channel proteins (3, 4)
222 and primary cilia (49) because they have been widely implicated in flow sensing in the
223 cardiovascular system (3, 50). We used established mutant lines for the stretch sensitive
224 channels *Trpp2*, *Trpv4*, *Piezo1*, *Piezo2a* and *Piezo2b* (4, 51, 52) and iguana (*Dzip1*) (53)
225 which is responsible for ciliogenesis in the cardiovascular system (54). We found that all
226 of these mutants showed normal Ca^{2+} activation (Fig. S7, A and B). These results were

227 confirmed by the fact that gadolinium ion (Gd^{3+}), a non-specific stretch-sensitive channel
228 blocker, did not suppress the Ca^{2+} influx significantly (Fig. S7C). These results suggest
229 that primary cilia and stretch sensitive channels are not the main regulators of the Ca^{2+}
230 oscillations observed in EdCs.

231

232 Considering none of the expected stretch sensitive channels affected calcium oscillations,
233 we turned to paracrine signals potentially released in response to mechanical forces.

234 Previous studies have shown that Adenosine 5' triphosphate (ATP) is released in cultured
235 endothelial cells in response to mechanical stimuli (16). As a response, ATP activates

236 Ca^{2+} signaling via an increase of the permeability of cations in purinergic receptor P2X
237 channels (55) (Fig. 4A). We thus hypothesized that intracellular Ca^{2+} fluxes are dependent

238 on ATP levels. ATP can be generated by endothelial mitochondria (56). Accordingly, we
239 found that the Ca^{2+} influx in EdCs of the AVC was abolished when cytosolic ATP levels

240 are depleted by oligomycin A, a mitochondrial ATP synthase inhibitor (Fig. S7D). We
241 next investigated whether extracellular ATP is able to alter Ca^{2+} influx in EdCs by

242 microinjecting oligomycin A, apyrase (an ATPase) and ATP γ S (an ATP analog) into the
243 cardiac lumen (Fig. 4B, and Movie S8). After both oligomycin A and apyrase injection,

244 we found that the Ca^{2+} influx was significantly suppressed in the EdCs of the AVC;
245 conversely, ATP γ S significantly increased the amount of Ca^{2+} influx (Fig. 4C, and Fig.

246 S7, E to G). In addition, ATP γ S led to a significant increase of both the number of cells
247 displaying Ca^{2+} spikes and the Ca^{2+} oscillation frequency in the EdCs (Fig. S7, H and I).

248 Importantly, the heart rate and the cell viability were not affected by these treatments,
249 suggesting that none of them altered the mechanical forces associated with heart function.

250 These results indicate that extracellular ATP is the trigger of Ca^{2+} signaling in EdCs in

251 response to flow.

252

253 The requirement of extracellular ATP for the Ca^{2+} influx in EdCs prompted us to
254 investigate the involvement of known ATP dependent channels such as P2X channels that
255 are activated by disturbed flows in response to ATP release in endothelial cells (57, 58).

256 We first examined whether P2X (P2rx in zebrafish) channels are expressed in the EdCs.

257 We found that *p2rx1*, *p2rx4a* and *p2rx7* transcripts are present in the endocardial cells of
258 the heart at 48 hpf and 72 hpf (Fig. S8, A and B). Thus P2rx expression is not restricted

259 to the AVC. Treatment against antagonists of P2X1, 4 and 7 decreased the number of
260 Ca^{2+} spikes in the EdCs (Fig. S8C). In line with this result, the embryos overexpressed a

261 dominant-negative form of either human *P2X4* (*hP2X4C353W*) or zebrafish *p2rx4a*
262 (*zP2rx4aC365W*) mRNA, as well as *p2rx4a* morphants, displayed a significant decrease

263 in the number of Ca^{2+} spikes in EdCs without affecting heartbeat (Fig. 4D, and Fig. S8,

264 D to G, and I). Overall, these results show that the Ca^{2+} influx in EdCs is modulated by
265 P2X channels in response to changes in extracellular ATP levels.

266 To understand how the activation and inhibition of P2X-mediated ATP signaling could

267 affect valve formation, we first assessed how altering calcium oscillations translate into
268 changes in gene expression. We tested whether P2X channels are involved in modulating

269 Nfat activity in EdCs. Although embryos treated with combinations of P2X1, 4 and 7

270 antagonists, combinations of P2X4 with P2Y2 antagonists, P2X4 antagonist, or P2Y2

271 antagonist significantly suppressed the Nfat reporter activation, the other P2X/P2Y

272 antagonists had no significant effect (Fig. S9, A and B). Furthermore, injection of a

273 dominant-negative form of *p2rx4* mRNA significantly suppressed reporter expression

274 (Fig. 4E and Fig. S8H), which correlates with abnormal Ca^{2+} activation (Fig. 4D and Fig.

275 S8G). Although Vegf signaling is known to activate Nfat signaling (59), Ki8751, a Vegfr2
276 inhibitor, had no effect on both Nfat reporter expression and Ca²⁺ activation in the EdCs
277 (Fig. S9, A to D). Together, these results suggest that P2X and P2Y receptors coordinately
278 modulate Nfat activity in the EdCs independently of VEGF signaling. In addition, we
279 found that the Nfat activity in the endocardium seems unrelated to the tyrosine
280 phosphorylation of Nfat determined by treatment of Janex-1 inhibiting jak3 which
281 specifically phosphorylates Nfat tyrosine (Fig. S9, A and E).

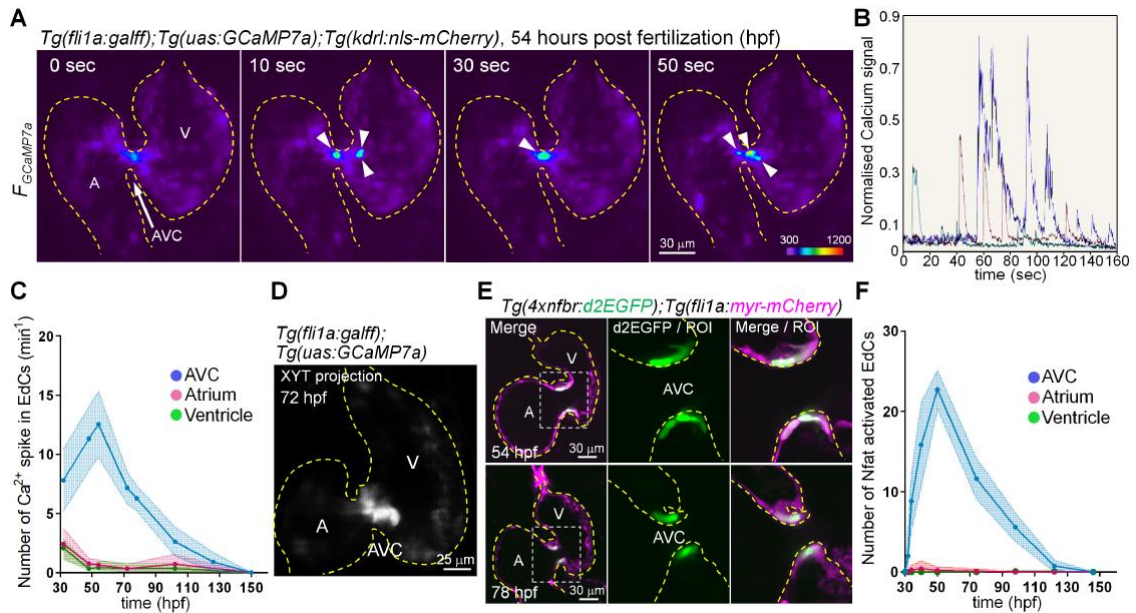
282 We finally tested the valve phenotype in the embryos with suppressed extracellular ATP
283 signaling. Although we found that Twist1b-positive cells localized in the endocardium,
284 they were mis-localized when p2rx function was inhibited (Fig. 4F and Fig. S10, A and
285 B). In addition, embryos displayed abnormal valve structures with incomplete
286 morphogenesis of the valve and absence of leaflet formation (Fig. 4G). We additionally
287 found that endocardial cells were excluded from the luminal part of the valve when Nfat
288 activity is suppressed in these cells (Fig. S10, C and D). Altogether these results confirm
289 that P2X functions acts upstream of Nfat activity to control EndoMT necessary for the
290 valve development.

291

292 Mechanical forces have been implicated in a broad range of events during embryonic
293 development (60-62). The presented work reframes our view of how endothelial cells
294 interpret mechanical forces and supports the intriguing possibility that valve formation is
295 mainly defined by the mechanosensitive inputs resulting from the local tissue constraints
296 and flow forces (26, 44, 63-65). Piezo and Trp channels are well established stretch
297 sensitive channels involved in cardiovascular morphogenesis and valve development
298 through the Notch and *klf2a-Wnt9b* pathway (4, 5, 51, 66, 67). Our work identifies ATP

299 as an additional mechanosensitive paracrine signal by which hemodynamic forces can
300 direct heart valve development, a compound that could be used to help grow heart valves
301 *in vitro* and may be involved in congenital heart valve defects.
302

303 **Figures and legends**

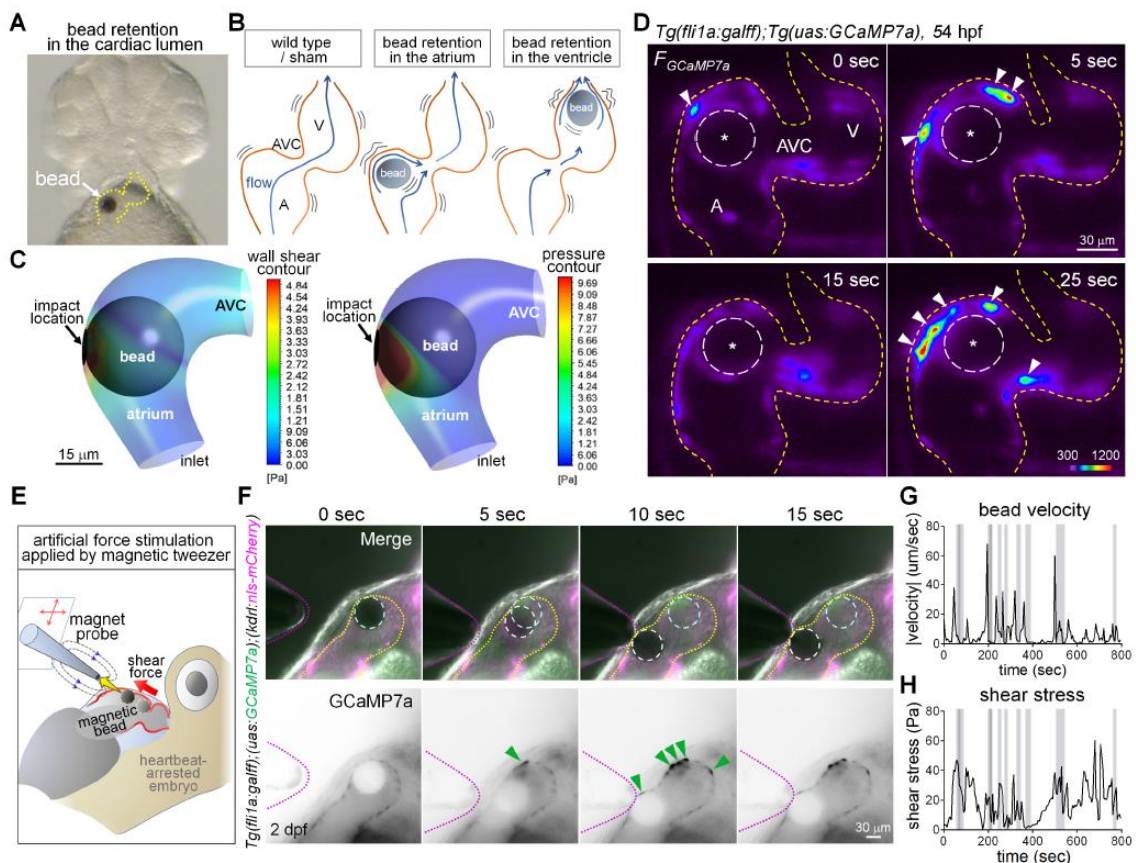


Fukui H et al., Fig. 1

304

305 **Fig. 1. Endogenous Ca^{2+} influx and Nfat signal activation occur in EdCs of the AVC**
 306 **during heart valve development. (A)** Representative single-scan beating heart images
 307 of the *Tg(fli1a:galff);Tg(uas:GCaMP7a);Tg(kdrl:nls-mCherry)* embryo at 54 hpf. Panels
 308 indicate the heat map-colored GCaMP7a images at indicated time points. Arrowheads
 309 and dashed lines indicate the activated GCaMP7a signal in the EdCs and the outline of
 310 the endocardium, respectively. **(B)** Normalized Ca^{2+} dynamics determined by
 311 $F_{GCaMP7a}/F_{nls-mCherry}$ in selected images that correspond to the same point of the cardiac
 312 cycle. Each color lines indicate the ratiometric change of individual cells (three cells).
 313 **(C)** The number of Ca^{2+} spike in EdCs of the atrium (red), ventricle (green) and AVC
 314 (blue) from 32 hpf to 150 hpf ($n > 5$). **(D)** XYT projection of GCaMP7a signal at 72 hpf
 315 in the same excitation position heart images for 60 sec (20 images). **(E)** Confocal single-
 316 scanned heart images of *Tg(4xnfbr:d2EGFP);Tg(fli1a:myr-mCherry)* embryo at 54 hpf
 317 (top panels, $n = 20$) and 78 hpf (bottom panels, $n = 12$). **(F)** The number of Nfat reporter

318 activated EdCs in the atrium (red), ventricle (green) and AVC (blue) from 30 hpf to 146
 319 hpf (n = 12). In the following graphs, A, V and AVC indicate the atrium, ventricle, and
 320 atrio-ventricular canal, respectively. Images were taken ventral view and anterior to the
 321 top unless otherwise described.
 322

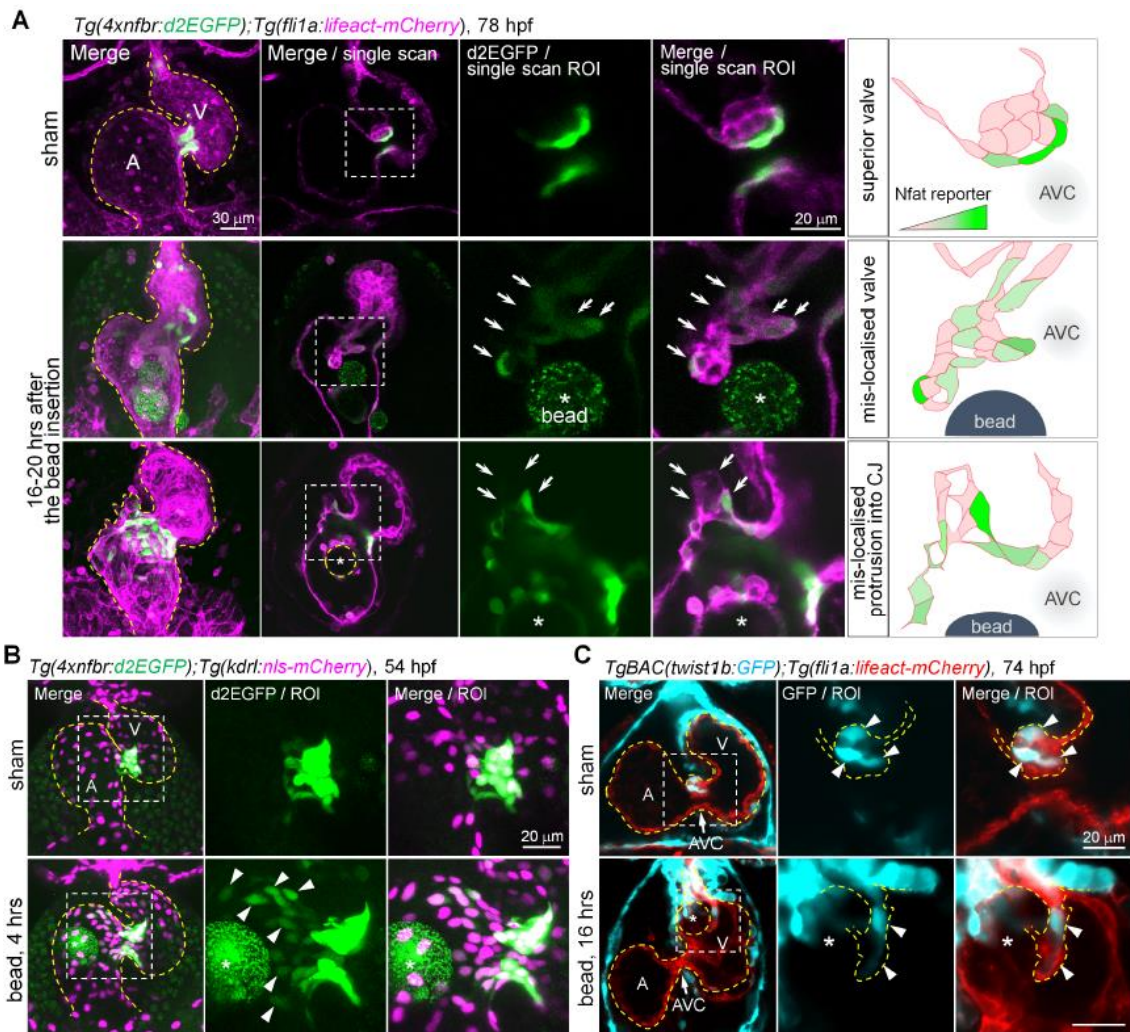


Fukui H et al., Fig. 2

323
 324 **Fig. 2. Force directly triggers Ca^{2+} influx in EdCs of zebrafish heart.** (A)
 325 Representative image of bead implantation into the heart. Yellow dotted lines depict the
 326 outline of the heart. (B) Schematics of bead retention. (C) 3D simulation of wall shear
 327 stress (left) and pressure (right) in when the bead is close to the impact location. Force
 328 intensities are indicated by color. Clear circles indicate a bead. (D) Representative beating
 329 heart images of the embryo grafted with a bead (dashed circle with asterisk) at 54 hpf.

330 Arrowheads and yellow dashed lines indicate the GCaMP7a signal in the EdCs and the
331 outline of endocardium, respectively. (E) Schematic of magnetic tweezer-based force
332 application to a zebrafish heart. (F) Representative single-scan images of arrested heart
333 of a *Tg(fli1a:galff);Tg(uas:GCaMP7a);Tg(kdrl:nls-mCherry)* embryo grafted with a
334 magnetic bead (dashed white circle; the original position is depicted as a dashed cyan
335 circle) pulled by the magnetic probe (dotted magenta lines) at 2 dpf. Green arrowheads
336 and dotted yellow lines indicate the GCaMP7a signal in EdCs and the outline of
337 endocardium, respectively. Images are left view of the embryo (N = 3, yielding similar
338 results). (G), (H) Quantification of bead velocity (G) and shear stress (H) applied by the
339 magnetic tweezer shown in movie [S7](#). The grey shades represent the period of activated
340 GCaMP7a signal in EdCs.

341



Fukui H et al., Fig. 3

342

343 **Fig. 3. Artificial forces lead to the formation of valve like structures. (A)**

344 Representative confocal images of *Tg(4xnfr:d2EGFP);Tg(fli1a:lifect-mCherry)*

345 embryo in sham-treatment (n = 11) and in 16-20 hours after retention of bead at 78 hpf (n

346 = 8). The most-right panels indicate the schematics of superior valve (top), mis-localised

347 valve (middle) and mis-localised protrusion into cardiac jelly (bottom row, arrowheads)

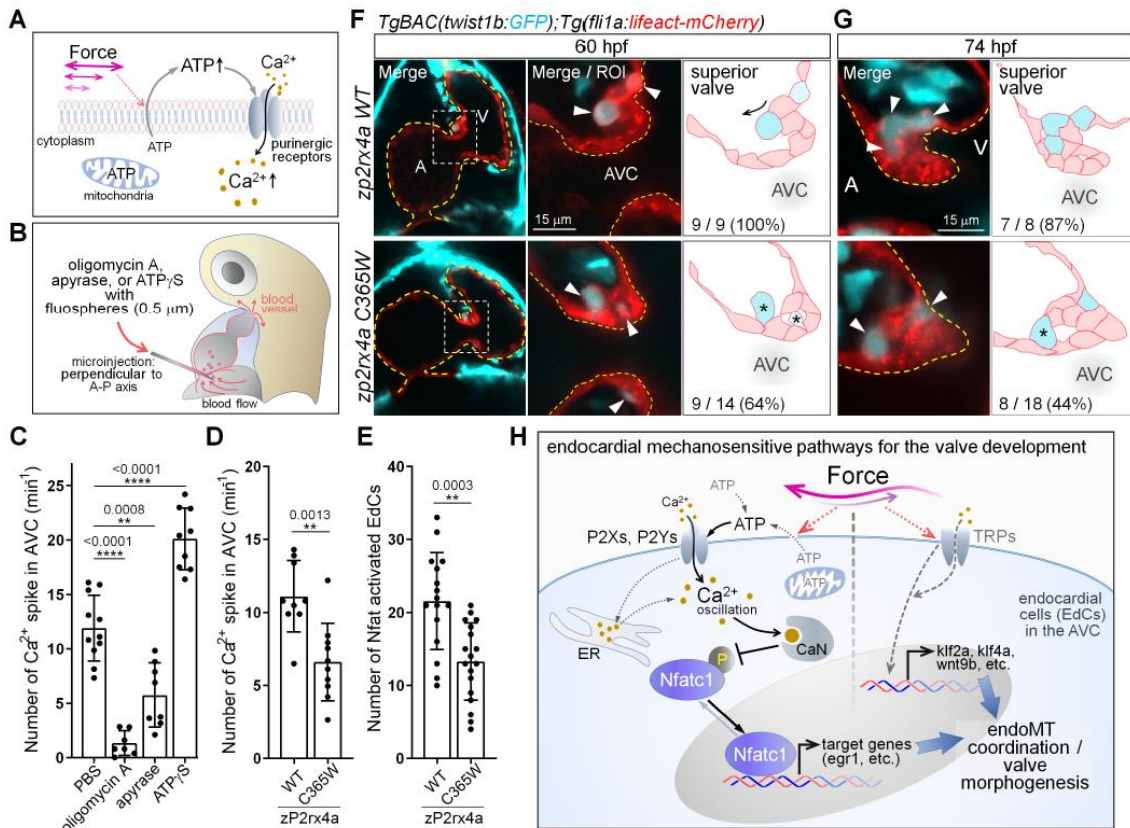
348 with Nfat reporter intensity (N > 5, yielding similar results individually). Arrows indicate

349 the ectopic structure induced by bead manipulation. **(B)** Representative confocal images

350 (54 hpf) of *Tg(4xnfr:d2EGFP);Tg(kdrl:nls-mCherry)* embryo in 4 hours after sham-

351 treatment (n = 7) or bead grafting (n = 13). The experiment was performed independently

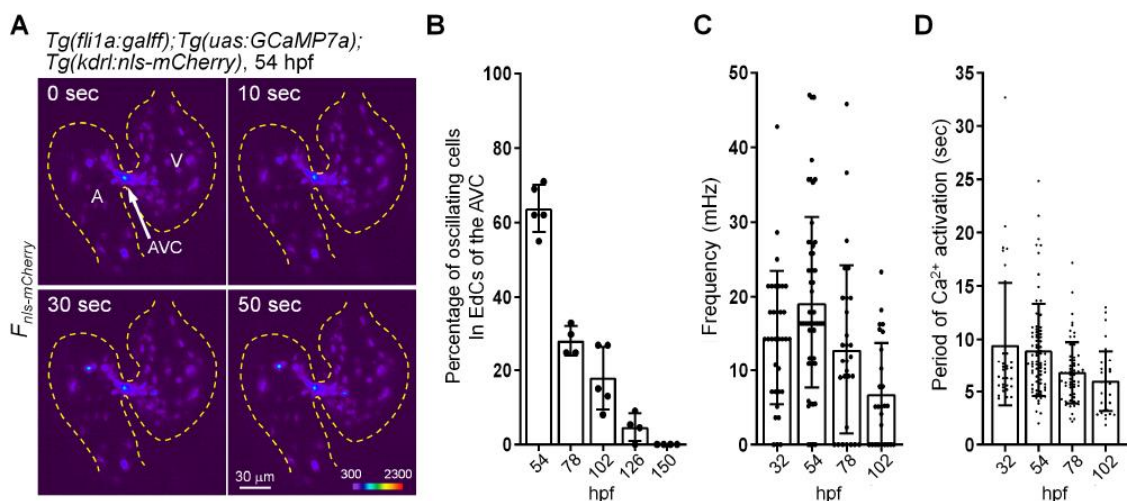
352 four-times, yielding to similar results. Arrowheads indicate the ectopic expression of Nfat
 353 reporter in EdCs. (C) Representative confocal images of
 354 *TgBAC(twist1b:GFP);Tg(fli1a:lfeact-mCherry)* embryo in sham-treatment (n = 10) and
 355 in 16 hours after retention of bead at 74 hpf (n = 7). Arrowheads indicate the Twist1b
 356 expression in EdCs. Yellow dashed lines depict the outline of the endocardium and
 357 demonstrating that superior valve in top panels and ectopic valve in bottom panels.
 358 Asterisks and dashed circles indicate the grafted bead in the heart lumen.
 359



Fukui H et al., Fig. 4

360
 361 **Fig. 4. Extracellular ATP and P2rx channels function proper valve development.** (A)
 362 Schematic of Ca²⁺ influx via extracellular ATP-dependent P2XRs activation. (B)
 363 Schematic of microinjection into cardiac lumen. (C) The number of Ca²⁺ spikes in EdCs

364 of the AVC for PBS (n = 11), oligomycin A (n = 7) apyrase (n = 8) and ATP γ S (n = 9)
 365 injected embryos at 54 hpf. (D), (E) The number of Ca²⁺ influxes (D) and Nfat reporter
 366 activation (E) in EdCs of the AVC for embryos injected with *zp2rx4aWT* (n = 9 in [D]; n
 367 = 16 in [E]) and *zp2rx4aC365W* mRNA (n = 10 in [D]; n = 18 in [E]) at 54 hpf. (F), (G)
 368 Representative confocal images of *TgBAC(twist1b:GFP);Tg(fli1a:lifect-mCherry)*
 369 embryo injected with *zp2rx4aWT* (n = 9 in [F]; n = 8 in [G]) and *zp2rx4aC365W* mRNA
 370 (n = 14 in [F]; n = 16 in [G]) at indicated time points. Arrowheads indicate the Twist1b
 371 expression in the EdCs. Yellow dashed lines as the outline of the endocardium and
 372 schematics of the superior valve in the right panels. Asterisks indicate the EdCs with an
 373 ectopic Twist1b expression that protruded from incorrect region. Arrow indicate cell
 374 movements to the cardiac jelly. (H) Schematic of endocardial mechanosensitive signal
 375 pathways for the valve development. Note that force triggers (ATP)-transducer (Ca²⁺)-
 376 decoder (NFAT) system which is independent of the *klf2a/klf4a* transcription activation.
 377



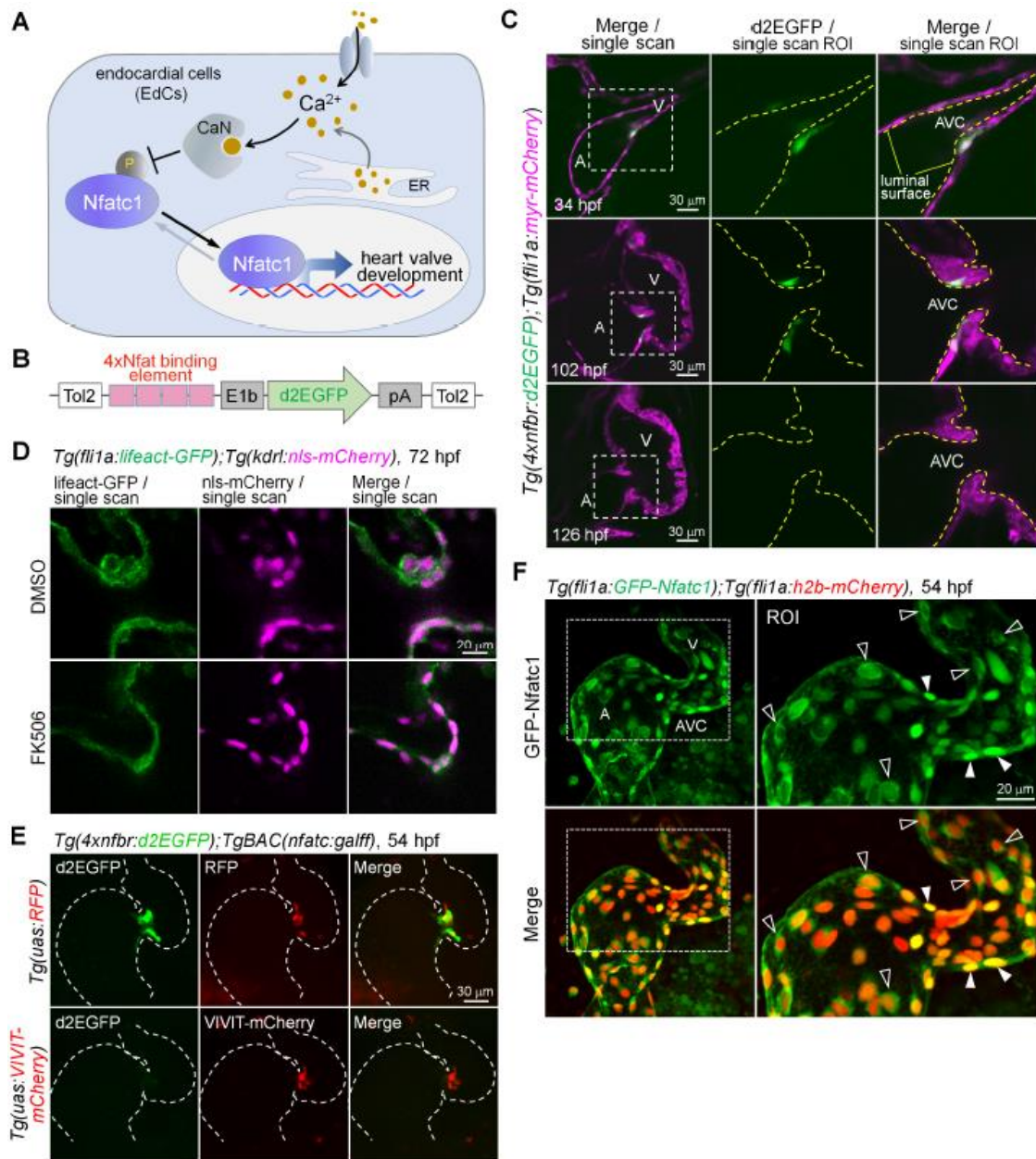
Fukui H et al., Fig. S1

378

379 **Fig. S1. Characterization of Ca²⁺ influx in EdCs during heart valve development.**

380 (A) Representative single-scan beating heart images of the
381 *Tg(fli1a:galff);Tg(uas:GCaMP7a);Tg(kdrl:nls-mCherry)* embryo at 54 hpf. Panels
382 indicate the heat map-colored nls-mCherry images at indicated time points. Yellow
383 dashed lines indicate the outline of the endocardium. (B) Quantification of the percentage
384 of Ca²⁺ oscillating cells in EdCs of the AVC at indicated time points: 54 hpf, n =5; 78
385 hpf, n = 4; 102 hpf, n = 5; 126 hpf, n = 4; 150 hpf, n = 4. (C) Frequency of Ca²⁺ spikes at
386 several time points: 32 hpf, n = 34; 54 hpf, n = 56; 78 hpf, n = 29; 102 hpf, n = 29. (D)
387 Quantification of the Ca²⁺ signal action period at several time points: 32 hpf, n = 45; 54
388 hpf, n = 77; 78 hpf, n = 62; 102 hpf, n = 37. In the following graphs, A, V and AVC
389 indicate the atrium, ventricle, and atrio-ventricular canal, respectively. Images were taken
390 from ventral view and anterior to the top unless otherwise indicated.

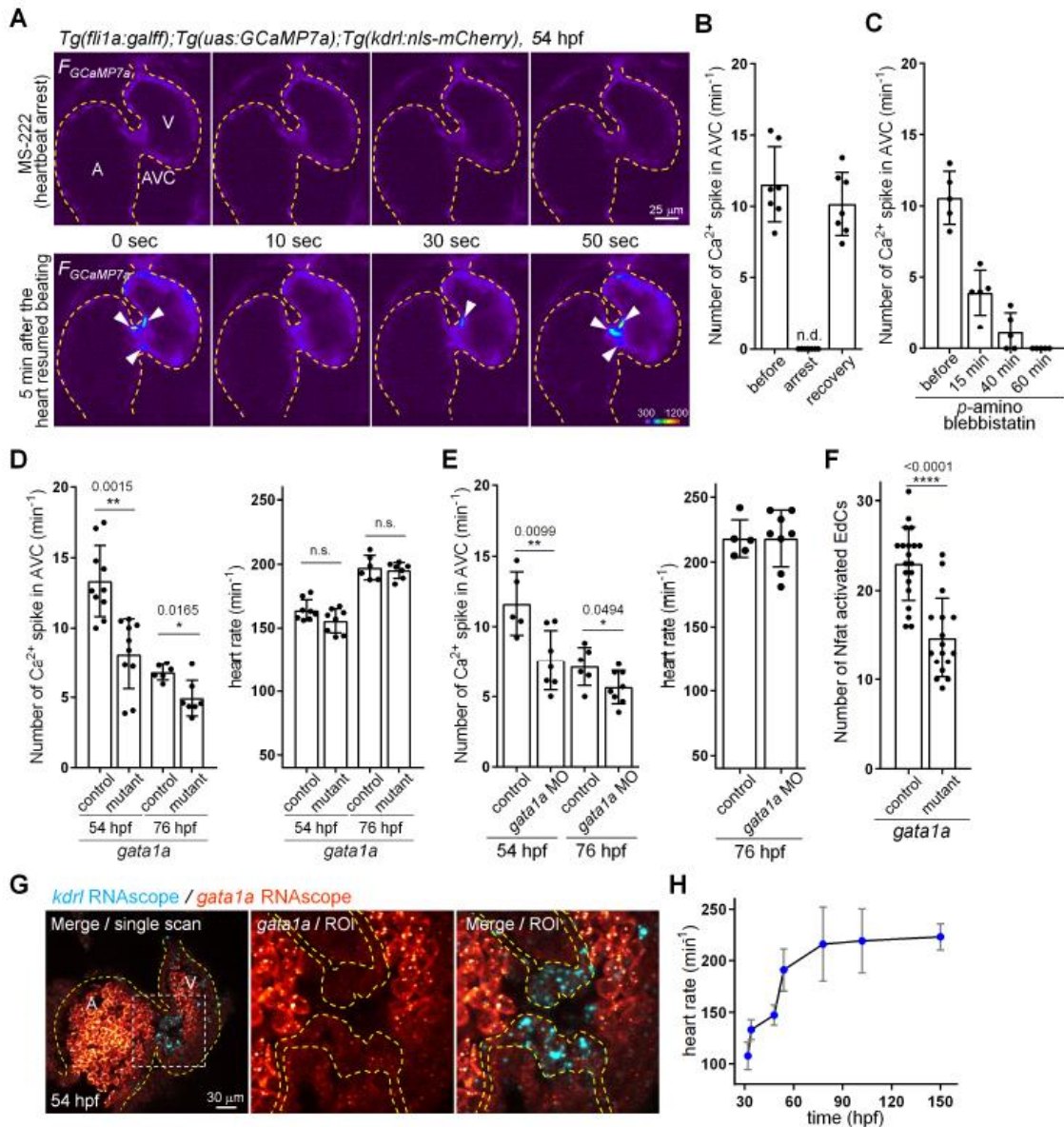
391



Fukui H et al., Fig. S2

392
 393 **Fig. S2. Characterization of Nfat reporter during heart valve development.** (A)
 394 Schematic of Nfat signal activation via Ca^{2+} influx in EdCs. (B) Schematic of the reporter
 395 construct for monitoring Nfat signal activation. (C) Representative heart images of
 396 *Tg(4xnfbr:d2EGFP);Tg(fli1a:myr-mCherry)* embryo at 34 hpf, 102 hpf and 126 hpf (n =
 397 14). Yellow dashed lines indicate the luminal surface of the EdC layer. (D) AVC region
 398 of *Tg(fli1a:lifect-GFP);Tg(kdrl:nls-mCherry)* embryo at 72 hpf treated with DMSO (n

399 = 6) or FK506 (n = 6). Note that FK506 treatment blocks EdC migration into cardiac jelly
400 in the AVC. (E) Representative embryonic heart images of
401 *Tg(4xnfbr:d2EGFP);TgBAC(nfatc1:galff)* crossed with *Tg(uas:RFP)* (n = 8) or
402 *Tg(uas:VIVIT-mCherry)* (n = 11) at 54 hpf. Note that VIVIT-mCherry suppresses
403 d2EGFP expression. The experiment was performed independently three times, each
404 yielding similar results. (F) Representative confocal scanned 3D stack images of 54 hpf
405 *Tg(fli1a:GFP-Nfatc1);Tg(fli1a:h2b-mCherry)* embryonic heart (n = 7). Closed
406 arrowheads and open arrowheads indicate the representative nuclear- and cytoplasmic -
407 localised GFP-Nfatc1, respectively. The experiment was performed independently three-
408 times, each yielding similar results.
409



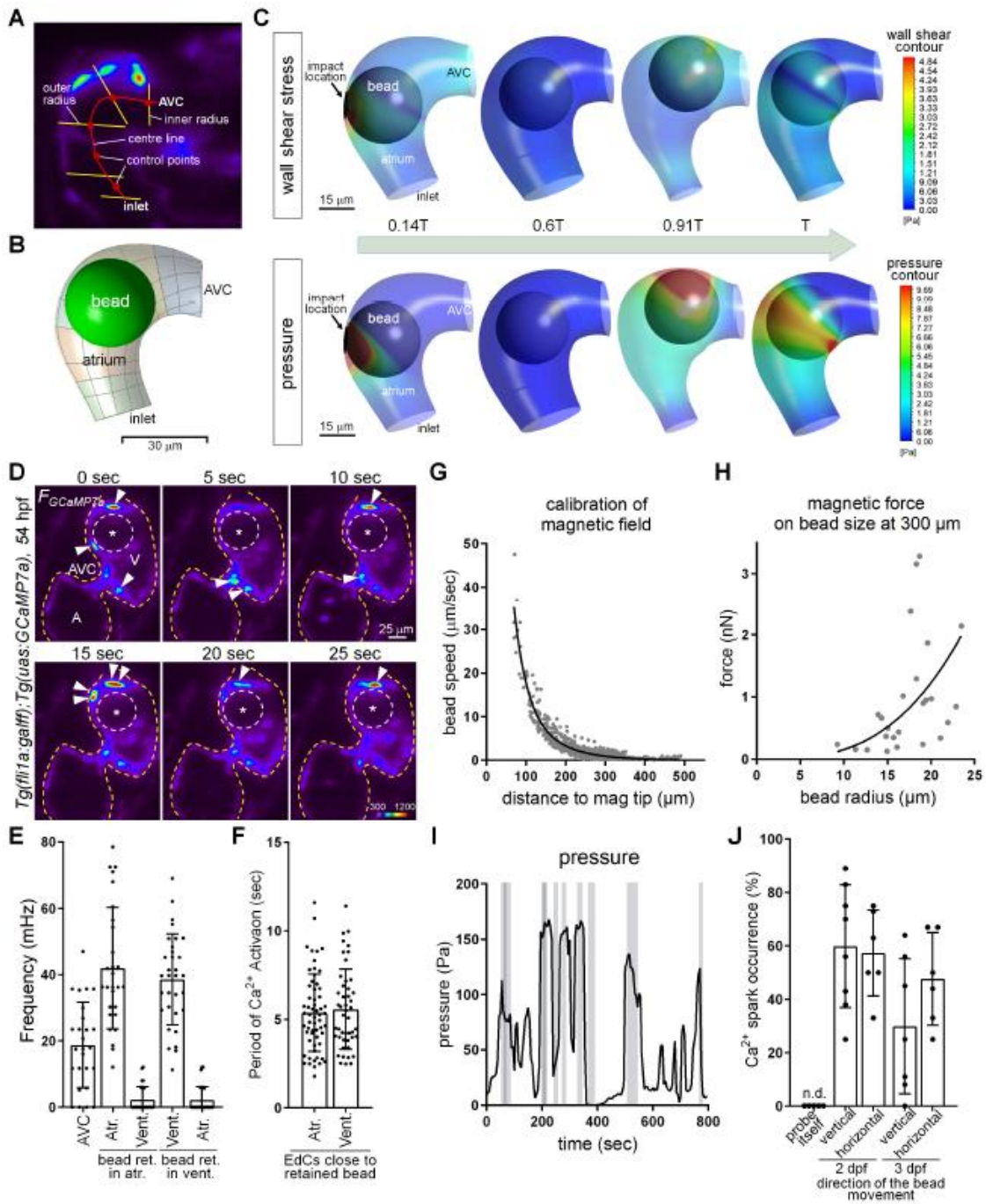
410

Fukui H et al., Fig. S3

411 **Fig. S3. Heartbeat and fluid shear forces control the Ca^{2+} influx in EdCs of the AVC.**

412 (A) Representative single-scan heart images of the
 413 *Tg(fli1a:galff);Tg(uas:GCaMP7a);Tg(kdr1:nls-mCherry)* embryo in a heart arrest
 414 condition by treatment with MS-222 (top panels) and in 5 min after heart resumed beating
 415 by wash-out of MS-222 (bottom panels) at 54 hpf. Panels indicate the heat map-colored
 416 GCaMP7a images at indicated time points. Arrowheads and dashed lines indicate the

417 activated GCaMP7a signal in the EdCs and the outline of endocardium, respectively. **(B)**
418 The number of Ca²⁺ spikes in EdCs of the AVC at 54 hpf. GCaMP7a signals were imaged
419 before heart arrest, during heart arrest by treatment of MS-222 (tricaine), and 5 min after
420 the heart resumes beating (n = 7). **(C)** Quantitative analyses of the number of Ca²⁺ spike
421 at the indicated time after the treatment of p-amino-blebbistatin at 54 hpf (n = 5). **(D)** The
422 number of Ca²⁺ spikes in EdCs of the AVC (left) and the heartrate (right) of *gatal* mutant
423 embryos at 54 hpf and 76 hpf. Control embryos (54 hpf, n = 10; 76 hpf, n = 6) and *gatal*
424 mutant embryos (54 hpf, n = 10; 76 hpf, n = 7) were determined by presence or absence
425 of blood cell circulation. **(E)** Quantitative analyses of the number of Ca²⁺ spikes in EdCs
426 of the AVC at 54 hpf and 76 hpf (left) and heart rate at 76 hpf (right) of embryos injected
427 with *control* MO (54 hpf, n = 5; 76 hpf, n = 6) or *gatal* MO (54 hpf, n = 7; 76 hpf, n =
428 8). **(F)** Quantitative analyses of the number of Nfat activated EdCs in *gatal* mutant
429 embryos at 54 hpf (control, n = 20; mutant, n = 17). **(G)** Representative images of
430 RNAscope analyses using *kdrl* with *gatala* probes in 54 hpf embryos (n = 6). Dashed
431 line in the single scan images and the ROI images indicate the outline of the heart and the
432 endocardium, respectively. The experiment was performed independently twice, yielding
433 similar results. **(H)** Quantitative analyses of the heart rate from 32 hpf to 150 hpf (n = 5).
434



Fukui H et al., Fig. S4

435

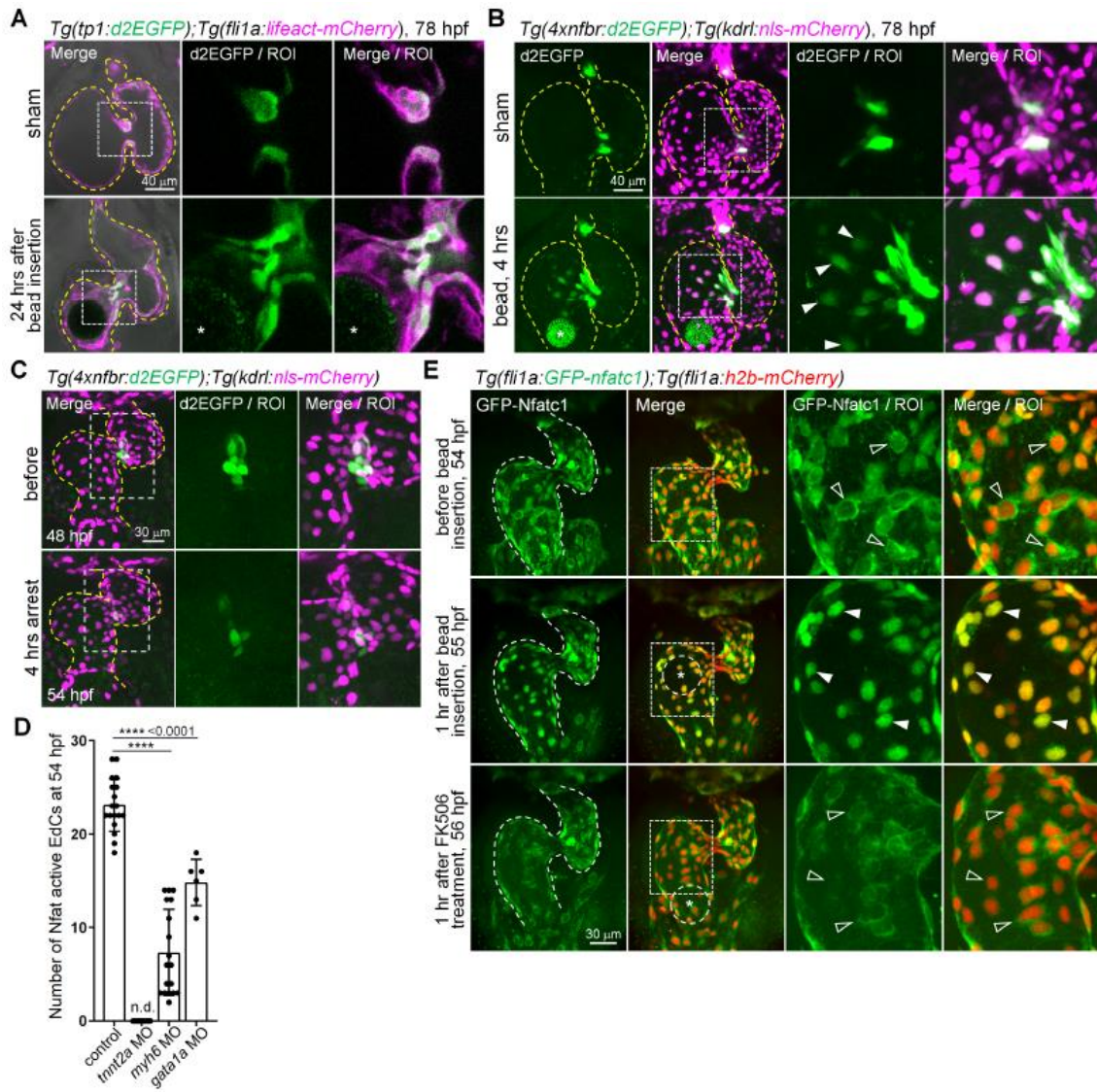
436 **Fig. S4. Retention of a bead in the cardiac lumen exerts forces on EdCs. (A)**

437 **Estimated 3D-reconstruction of atrial-chamber and magnetic-bead for the simulation. (B)**

438 **Motion-waveform of the magnetic-bead obtained from the video, plotted in normalized**

439 **distance (X-coord) and cardiac-cycle duration (T). (C) 3D simulation of wall shear stress**

440 (top panels) and pressure (bottom panels) in the bead manipulated in the atrium. Force
441 intensities are shown in the heat map color. Clear circles indicate a 30 μm bead. **(D)**
442 Representative single-scan beating heart images of the embryo retained with magnetic
443 bead (dashed circle with asterisk) into ventricular lumen at 54 hpf. Panels indicate the
444 heatmap-colored GCaMP7a images at the indicated time points. Arrowheads and yellow
445 dashed lines depict the activated GCaMP7a signal in EdCs and the outline of endocardium,
446 respectively. **(E)** Quantitative analyses for the frequency of Ca^{2+} oscillation in sham EdCs
447 of the AVC ($n = 26$), EdCs close to grafted bead (atrium, $n = 28$; ventricle, $n = 32$) and
448 EdCs of the other chamber which does not have a bead (atrium, $n = 28$; ventricle, $n = 30$).
449 **(F)** Quantitative analyses for the period of Ca^{2+} activation in EdCs close to retained bead
450 in the atrium ($n = 59$) or the ventricle ($n = 47$). **(G)** Calibration of magnetic field. Plot of
451 the velocity with the distance between bead and magnet tip calculated by using 2.8 μm
452 bead. **(H)** Magnetic force calibration on bead size at 300 μm distance. **(I)** Quantification
453 of the pressure into EdCs applied by the magnetic tweezer shown in movie S7. The grey
454 shades represent the period of activated GCaMP7a signal in EdCs. **(J)** Quantitative
455 analyses of the ratio of Ca^{2+} spark occurrence in EdCs triggered by the magnetic tweezer.
456 The direction of bead movement against the EdCs layer was classified as vertically (2 dpf,
457 $n = 8$; 3 dpf, $n = 7$) and horizontally (2 dpf, $n = 6$; 3 dpf, $n = 6$). Note that pushing by the
458 tip of the magnetic probe itself comes from the outside of the embryos was not triggered
459 the Ca^{2+} spark in EdCs ($n = 5$).
460

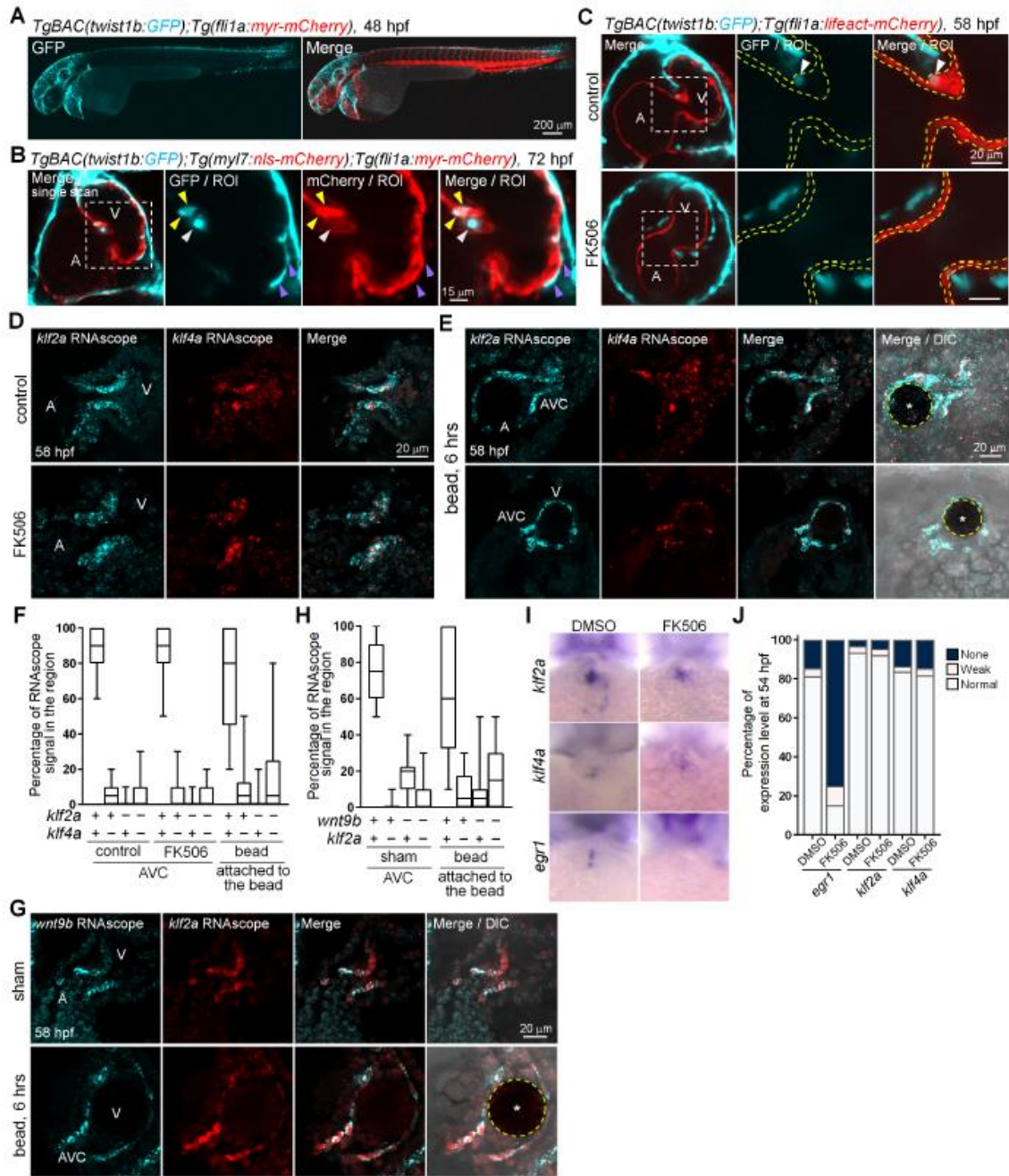


Fukui H et al., Fig. S5

461

462 **Fig. S5. Bead retention leads to the ectopic reporter activation.** (A) Representative
 463 single scanned confocal images of 78 hpf *Tg(tp1:d2EGFP);Tg(fli1a:lifact-mCherry)*
 464 embryonic heart in 24 hours after sham-treatment (n = 6) and bead grafting (n = 3). The
 465 experiment was performed independently twice, each yielding similar results. (B)
 466 Representative confocal scanned 3D stack images of 78 hpf
 467 *Tg(4xnfbr:d2EGFP);Tg(kdr:nls-mCherry)* embryonic heart in 4 hours after sham-
 468 treatment (n = 12) and bead grafting (n = 8). Arrowheads depict the activated Nfat reporter

469 in EdCs. The experiment was performed independently four-times, each yielding similar
470 results. (C) Representative confocal images of *Tg(4xnfbr:d2EGFP);Tg(kdrl:nls-*
471 *mCherry)* embryonic heart at 48 hpf (top panels, n = 5) and the same embryo after
472 heartbeat has been arrested using BDM for 4 hours (bottom panels, n = 5). The experiment
473 was performed twice yielding similar results. (D) Number of Nfat reporter activated EdCs
474 at 54 hpf in embryos injected with *control* MO (control, n = 7), *tnnt2a* MO (n = 10), *myh6*
475 MO (n = 18) and *gata1a* MO (n = 6). (E) Representative confocal scanned 3D stack heart
476 images of *Tg(fli1a:GFP-Nfatc1);Tg(fli1a:h2b-mCherry)* before bead insertion (top
477 panels, 54 hpf), with bead insertion for 1 hr (middle panels, 55 hpf), and 1 hr after FK506
478 treatment (bottom panels, 56 hpf) in the same embryos (n = 7). Closed arrowheads and
479 open arrowheads indicate the representative nuclear- and cytoplasmic-localised GFP-
480 Nfatc1, respectively. The experiment was performed independently three-times, each
481 yielding similar results. Yellow dashed lines indicate the outline of endocardium.
482



Fukui H et al., Fig. S7

483

484 **Fig. S6. Nfat activation is dispensable for the force-dependent *klf2a/klf4a* expression.**

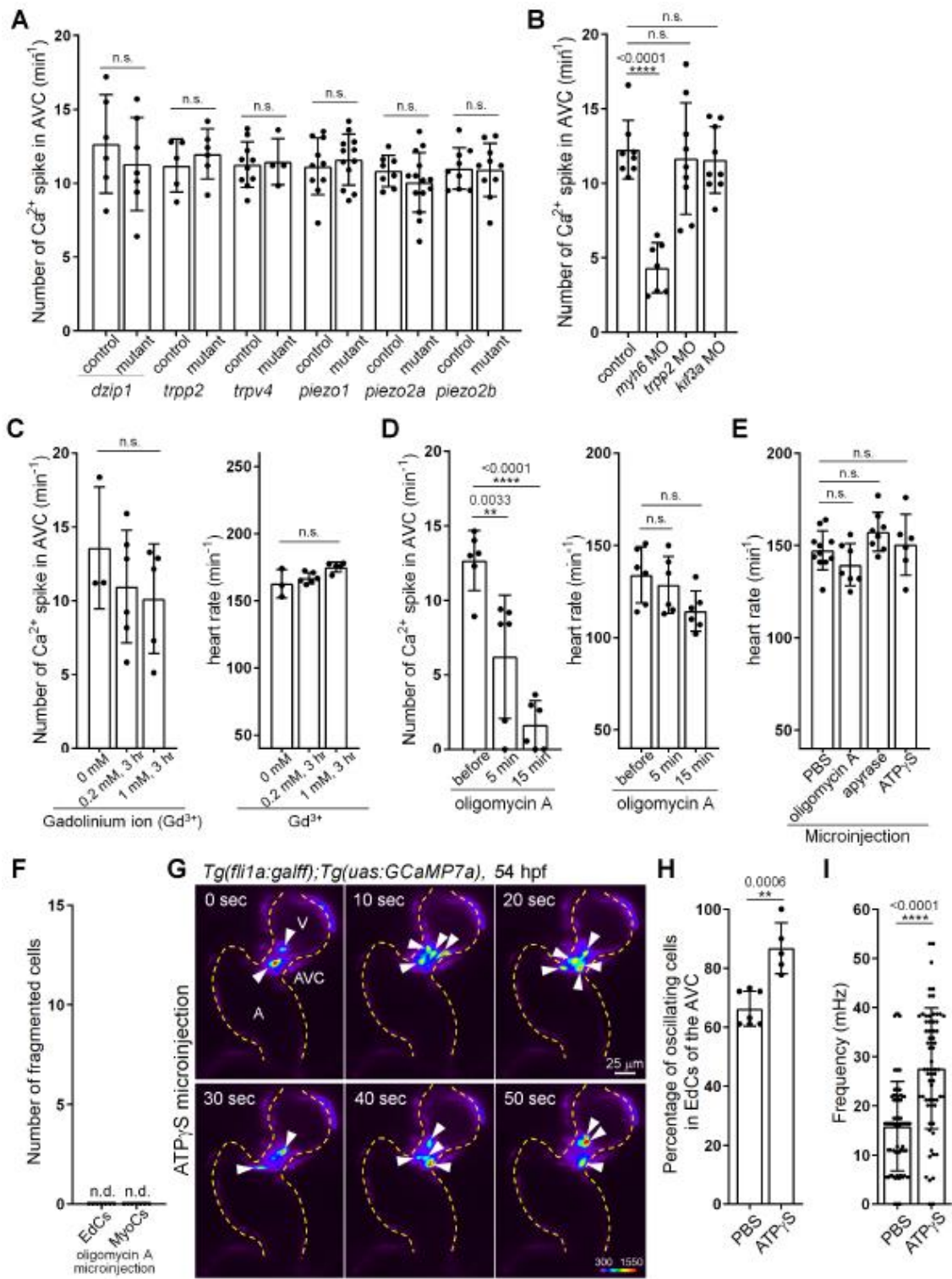
485 (A) Representative 3D stack confocal images of *TgBAC(twist1b:GFP);Tg(fli1a:myr-*

486 *mCherry)* embryo at 48 hpf. Anterior to the left (n = 3). (B) Representative single scanned

487 confocal heart images of *TgBAC(twist1b:GFP);Tg(myl7:nls-mCherry);Tg(fli1a:myr-*

488 *mCherry)* embryo at 72 hpf. White arrowheads, yellow arrowheads, and purple

489 arrowheads indicate the Twist1b positive cells in the endocardium, myocardium, and
490 epicardium, respectively (n = 4). (C) Representative single scanned confocal heart images
491 of *TgBAC(twist1b:GFP); Tg(fli1a:lfeact-mCherry)* embryo treated with DMSO (control
492 shown on top panels, n = 6) or FK506 (bottom panels, n = 6) at 58 hpf. Arrowheads and
493 yellow dashed lines indicate the Twist1b positive cell and the outline of endocardium,
494 respectively. The experiment was performed independently three-times, each yielding
495 similar results. (D), (E) Representative images of RNAscope analyses of 58 hpf embryos
496 treated with DMSO (control, n = 12, [D]), FK506 (n = 19, [D]) and bead insertion for 6
497 hrs (n = 13, [E]) using the *klf2a* with *klf4a* probes. (F), (H) Boxplot representing the ratio
498 of positive RNAscope signal in selected 10 voxels (5 μ m each) of the AVC (D in F; G in
499 H) and of the EdCs attached to the bead (E in F; G in H). (G) Representative images of
500 RNAscope analyses of 58 hpf embryos with sham treatment (n = 14), and bead insertion
501 for 6 hrs (n = 17) using the *klf2a* with *wnt9b* probes. Yellow dashed circles with asterisk
502 indicate the inserted bead in the cardiac lumen. (I), (J) Representative WISH images of
503 54 hpf embryos treated with DMSO or FK506 from 34 hpf to 54 hpf (I) and percentage
504 of expression level categorized for three patterns (normal, weak and none) (J). Following
505 anti-sense probes were used: *klf2a*, n = 122 (DMSO) and n = 127 (FK506); *klf4a*, n = 73
506 (DMSO) and n = 55 (FK506); *egr1*, n = 123 (DMSO) and n = 151 (FK506). The
507 experiment was performed independently four times, yielding similar results.
508

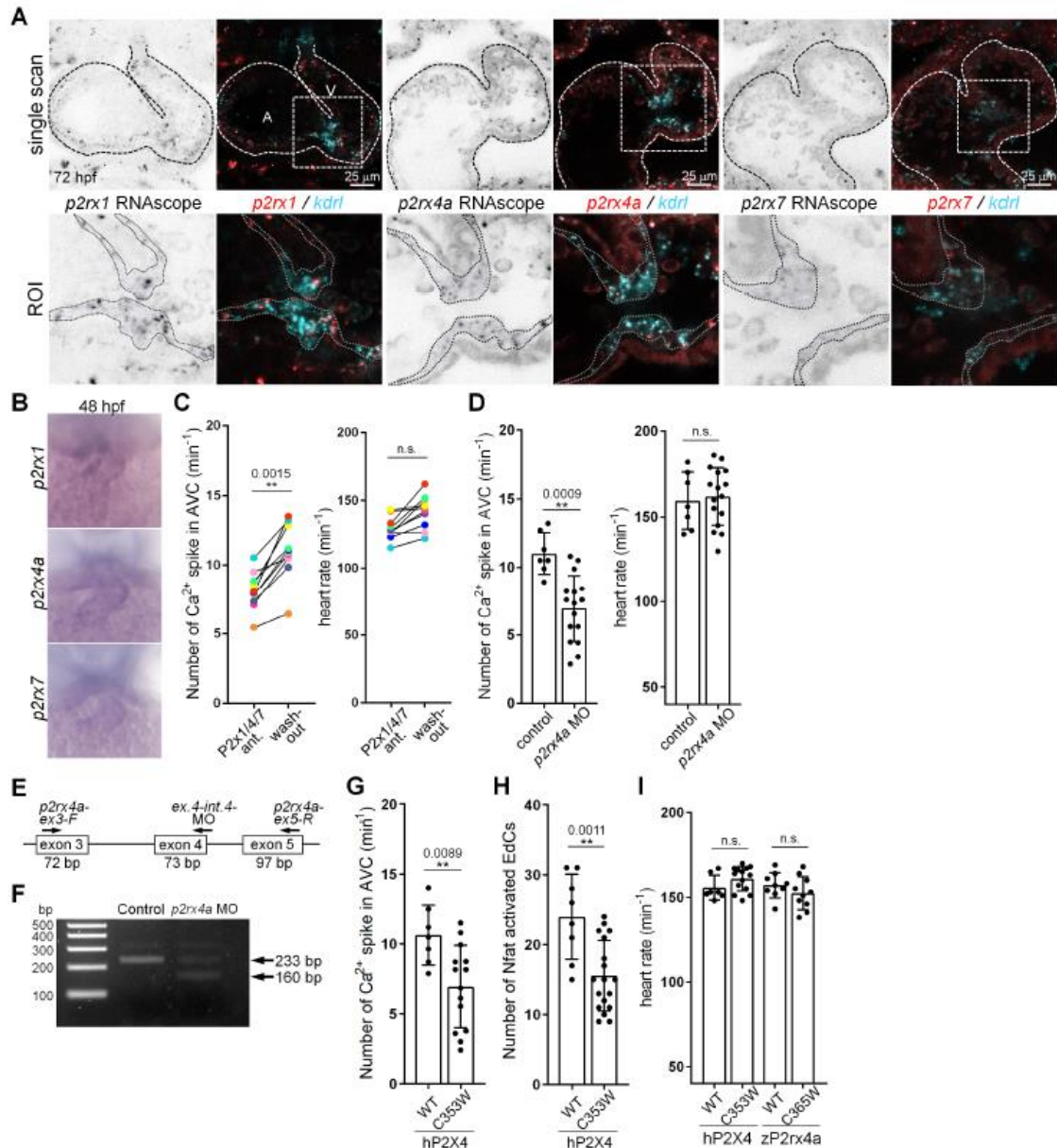


509

Fukui H et al., Fig. S8

510 **Fig. S7. Ca^{2+} influx in EdCs is regulated by extracellular ATP-dependent signaling.**

511 (A) Quantitative analyses of the number of Ca²⁺ spikes in EdCs of the AVC of *dzip1*,
512 *trpp2*, *trpv4*, *piezo1*, *piezo2a* and *piezo2b* mutant embryos at 54 hpf. Control embryos
513 represent the wild type and heterozygous embryos (*dzip1* control, n = 6; *dzip1* mutant, n
514 = 7; *trpp2* control, n = 5; *trpp2* mutant, n = 6; *trpv4* control, n = 10; *trpv4* mutant, n = 4;
515 *piezo1* control, n = 10; *piezo1* mutant, n = 12; *piezo2a* control, n = 8; *piezo2a* mutant, n =
516 14; *piezo2b* control, n = 9; *piezo2b* mutant, n = 10). (B) Quantitative analyses of the
517 number of Ca²⁺ spikes in EdCs of the AVC in embryos injected with *control* MO (n = 8),
518 *myh6* MO (n = 7), *trpp2* MO (n = 9) and *kif3a* MO (n = 9). (C) Quantitative analyses of
519 the number of Ca²⁺ spike in EdCs of the AVC (left) and heart rate (right) in embryos
520 treated with 0.2 mM (n = 6) and 1 mM (n = 5) GdCl₃ at 54 hpf (No treatment indicated
521 as 0 mM, n = 3). (D) The number of Ca²⁺ spikes in EdCs of the AVC (left) and heart rate
522 (right) at 54 hpf (n = 6) before, 5 min after, and 15 min after oligomycin A treatment. (E)
523 Quantitative analyses of the heart rate in for PBS (n = 11), oligomycin A (n = 7), apyrase
524 (n = 8) and ATPγS (n = 6) injected embryos at 54 hpf. (F) The number of fragmented
525 EdCs and MyoCs in embryos injected with oligomycin A (n = 7). (G) Representative
526 beating heart images of an embryo microinjected with ATPγS at 54 hpf. Panels indicate
527 the heat map-colored GCaMP7a images at indicated time points. Arrowheads and dashed
528 lines depict the activated GcaMP7a signal in EdCs and the outline of the endocardium,
529 respectively. (H), (I) Quantitative analyses of the percentage of Ca²⁺ oscillating cells in
530 EdCs of the AVC (PBS, n = 7; ATPγS, n = 5) (H) and the frequency of Ca²⁺ spikes (PBS,
531 n = 71; ATPγS, n = 66) (I) in embryos injected with PBS or ATPγS at 54 hpf.
532



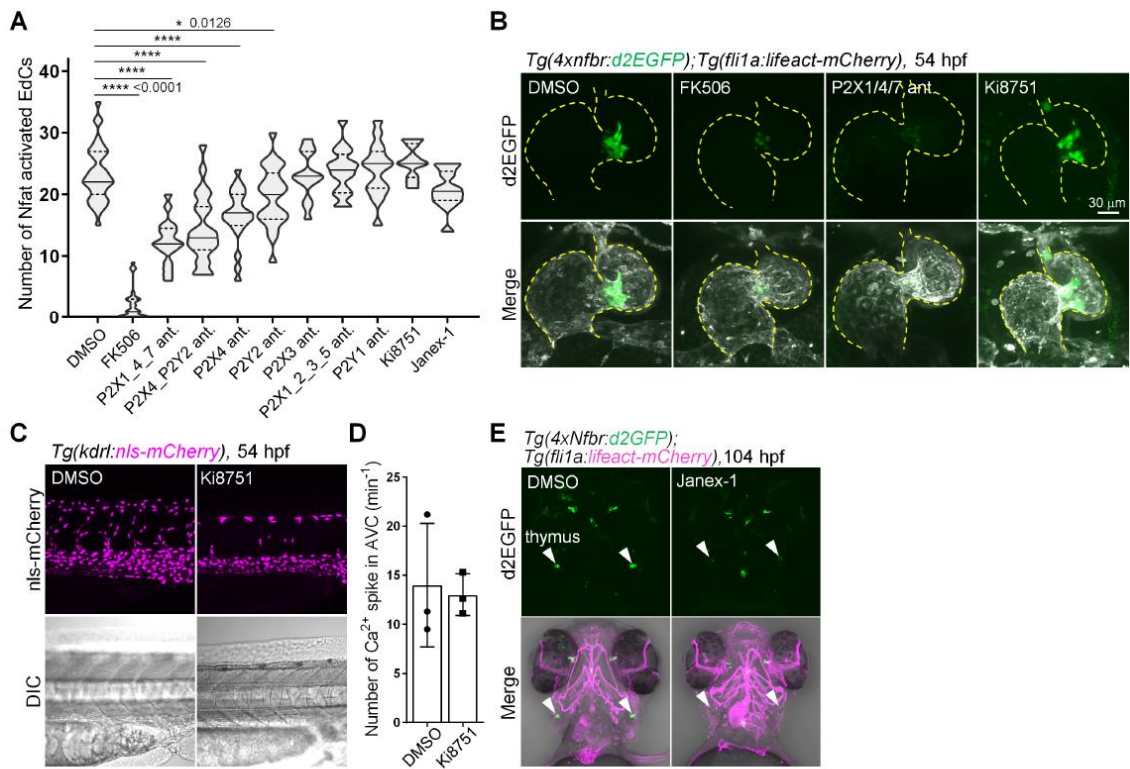
533

Fukui H et al., Fig. S9

534 **Fig. S8. Ca²⁺ influx and Nfat reporter activation are regulated by P2rx channels**
 535 **expressed in EdCs. (A)** Representative images of RNAscope analyses of 72 hpf embryos
 536 using the following RNAscope probes: *kdrl* with *p2rx1*, n = 10; *kdrl* with *p2rx4a*, n = 12;
 537 *kdrl* with *p2rx7*, n = 7. Dashed line in single scan images and the region between the
 538 dotted lines in ROI images indicate the outline of the endocardium and the endocardium,
 539 respectively. The experiment was performed independently twice, yielding similar results.

540 (B) Representative images of WISH analysis of 48 hpf embryos using the following anti-
541 sense probes: *p2rx1*, n = 20; *p2rx4a*, n = 24; *p2rx7*, n = 18. The experiment was performed
542 independently three times, yielding similar results. (C) The number of Ca²⁺ influxes in
543 EdCs of the AVC (left) and heart rate (right) for 60 min of each 10 μM of p2rx1_4_7
544 antagonists (NF023, 5-BDBD and A438079) treated embryos and wash-out embryos at
545 54 hpf embryos (n = 10). (D) Quantitative analyses of the number of Ca²⁺ spikes in EdCs
546 of the AVC (left) and heart rate (right) in embryos injected with *control* MO (n = 7) or
547 *p2rx4a* MO (n = 16) at 54 hpf. (E) Schematic of primer set and MO target site of *p2rx4a*.
548 (F) RT-PCR analysis to reveal the splicing-block by *p2rx4a* MO. Total RNA from
549 embryos injected with MOs at 48 hpf were collected and subjected RT-PCR. Note that
550 the samples injected with *p2rx4a* MO show the 160 bp band that is skipped in exon 4 of
551 *p2rx4a*. (G), (H) The number of Ca²⁺ influxes (G) and Nfat reporter activation (H) in
552 EdCs of the AVC for embryos injected with *hP2X4 WT* (n = 7 in [G]; n = 8 in [H]) and
553 *hP2X4C353W* (n = 14 in [G]; n = 18 in [H]) mRNA at 54 hpf. (I) Quantitative analyses
554 of the heart rate in embryos injected with *hP2X4 WT* (n = 7), *hP2X4C353W* (n = 14),
555 *zp2rx4aWT* (n = 9) and *zp2rx4aC365W* (n = 10) mRNAs at 54 hpf.

556

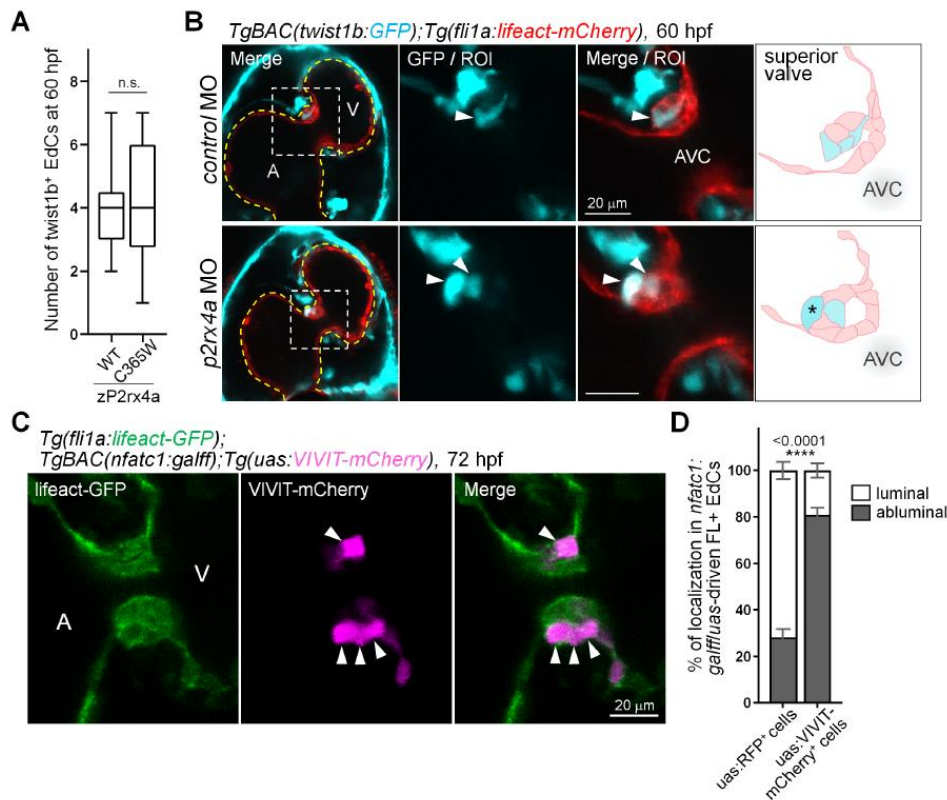


557

Fukui H et al., Fig. S10

558 **Fig. S9. Several P2Xs/P2Ys coordinately regulate Nfat activity in EdCs.** (A) Violin
 559 plot demonstrating the number of Nfat reporter activated EdCs at 52 hpf in control
 560 (DMSO, n = 37), FK506 (n = 12), P2X1_4_7 antagonists (n = 22), P2X4_P2Y2
 561 antagonists (n = 25), P2X4 antagonist (5-BDBD, n = 17), P2Y2 antagonist (AR-C
 562 118925XX, n = 23), P2X3 antagonist (A317491, n = 13), P2X1_2_3_5 antagonist
 563 (PPADS tetrasodium salt, n = 16), P2Y1 antagonist (BPT-U, n = 15), VEGFR2 inhibitor
 564 (Ki8751, n = 10) and Janex-1 (jak3 inhibitor, n = 12) treatment from 34 hpf to 54 hpf. (B)
 565 Confocal scanned images of *Tg(4xnfbr:d2EGFP);Tg(fli1a:lifeact-mCherry)* embryonic
 566 heart at 54 hpf treated with drugs from 34 hpf to 54 hpf (DMSO, n = 24; FK506, n = 12;
 567 P2X1_4_7 antagonists, n = 17; Ki8751, n = 10). Yellow dashed lines indicate the outline
 568 of the endocardium. (C) Representative images of *Tg(kdrl:nls-mCherry)* embryo at 54
 569 hpf treated with DMSO or Ki8751 from 34 hpf to 54 hpf (DMSO, n = 6; Ki8751, n = 6).

570 Note that Ki8751 significantly suppresses angiogenesis in the trunk area. Images are
 571 taken lateral view, anterior to the left. (D) Number of Ca²⁺ spikes in EdCs of the AVC in
 572 embryos at 54 hpf treated with DMSO (n = 3) or Ki8751 (n = 3) from 34 hpf to 54 hpf.
 573 (E) Representative images of *Tg(4xnfbr:d2EGFP);Tg(fli1a:lfeact-mCherry)* embryo at
 574 104 hpf treated with DMSO (n = 10) or Janex-1 (n = 10) from 36 hpf to 104 hpf. Note
 575 that Janex-1 significantly suppresses Nfat reporter activity in the thymocyte (arrowheads).
 576



577

Fukui H et al., Fig. S11

578 **Fig. S10. Nfat-suppressed EdCs are excluded for the luminal area of the AVC. (A)**
 579 Boxplot representing the number of *twist1b*⁺ EdCs of the AVC in embryos injected with
 580 *zp2rx4a*WT (n = 9) and *zp2rx4a*C365W (n = 14) mRNAs at 60 hpf. (B) Representative
 581 confocal images of *TgBAC(twist1b:GFP);Tg(fli1a:lfeact-mCherry)* embryo injected

582 with *control* MO (n = 6) and *p2rx4a* MO (n = 6) at 60 hpf. Arrowheads indicate the
583 *twist1b* expression in the EdCs. Yellow dashed lines depict the outline of the endocardium
584 and schematics of the superior valve demonstrate in the right panels. Asterisks indicate
585 the EdCs with an ectopic *twist1b* expression that protruded from the abnormal region. (C)
586 Representative images of *Tg(fli1a:lfeact-GFP);TgBAC(nfatc1:galff);Tg(uas:VIVIT-*
587 *mCherry)* embryo at 72 hpf. Arrowheads indicate the VIVIT-mCherry positive EdCs in
588 the abluminal region of the AVC. (D) Quantitative analyses of the luminal / abluminal
589 localisation ratio in the fluorescence positive EdCs under the *TgBAC(nfatc1:galff)* driver
590 crossed with *Tg(uas:RFP)* (left column, n = 19) and with *Tg(uas:VIVIT-mCherry)* (right
591 column, n = 23) at 72 hpf.

592

593

594 **Movie S1.** Single scanned live imaging video (10 msec / frame) of Ca^{2+} influx in EdCs
595 (black, *fli1a:galff, uas:GCaMP7a*) in a 54 hpf embryo. The video was taken ventral view
596 using lightsheet microscope, anterior to the top. Magenta arrowheads depict the activated
597 GCaMP7a signal in EdCs.

598

599 **Movie S2.** Artificially stopped XYtR heart video (original movie was taken by 20 msec
600 / frame) for ratiometric analysis of Ca^{2+} influx in EdCs (green, *fli1a:galff, uas:GCaMP7a*)
601 and nuclear-localised mCherry signal in EdCs (magenta, *kdrl:Nls-mCherry*) at 54 hpf
602 embryo (n = 3). The video was taken ventral view using the spinning disc microscope,
603 anterior to the top. White arrowheads indicate the activated GCaMP7a signal in EdCs.

604

605 **Movie S3.** Single scanned bright field video of the bead grafted embryo at 54 hpf. Ventral

606 view and anterior to the top.

607

608 **Movie S4.** 3D simulation video of wall shear stress in the bead grafted atrial heart region
609 **with dynamic wall motion** for one cardiac cycle. Shear force intensity was shown by the
610 heat map color.

611

612 **Movie S5.** Single scanned live imaging video (10 msec / frame) of Ca^{2+} influx in EdCs
613 (heat map color, *fli1a:galff,uas:GCaMP7a*) of the bead grafted embryo at 54 hpf. The
614 bead was retained in the atrium (yellow circle). Arrowheads depict the activated
615 GCaMP7a signal in EdCs. The video was taken ventral view using a lightsheet
616 microscope, anterior to the top.

617

618 **Movie S6.** Single scanned live imaging video (10 msec / frame) of Ca^{2+} influx in EdCs
619 (heat map color, *fli1a:galff,uas:GCaMP7a*) of the bead grafted embryo at 54 hpf. The
620 bead was retained in the ventricle (yellow circle). Arrowheads indicate the activated
621 GCaMP7a signal in EdCs. The video was taken ventral view using a lightsheet
622 microscope, anterior to the top.

623

624 **Movie S7.** Single scanned live imaging video (5 sec / frame) of Ca^{2+} influx in EdCs (green,
625 *fli1a:galff,uas:GCaMP7a*) and nuclear-localised mCherry signal in EdCs (magenta,
626 *kdrl:Nls-mCherry*) of the magnetic bead grafted embryo at 2 dpf, and the right panel is
627 the DIC image. The magnetic bead (64 μm) was retained in the atrium and the magnetic
628 tweezer was applied after arresting heartbeat. The video was taken left view using an
629 inverted epifluorescent microscope, anterior to the top. White arrowheads depict the

630 initiation of the activated GCaMP7a signal in EdCs.

631

632 **Movie S8.** Single scanned live imaging video (10 msec / frame) in injection of PBS and
633 fluospheres (black, 0.5 μm) into cardiac lumen of *Tg(fli1a:galff,uas:GCaMP7a)* embryo
634 at 54 hpf. The video was taken ventral view using a lightsheet microscope, anterior to the
635 top. Magenta arrowheads depict the moving fluospheres in response to the blood flow.

636

637

638 **Acknowledgements**

639 We thank the member's in J.V.'s lab and in N. Mochizuki's lab for discussion and
640 comments on the manuscript; the entire staff of the imaging facility and the fish facility
641 in IGBMC for their assistance; Y.Y.F. in Y.C.H. lab for tabulation of the simulation
642 results; M.S., A.C. and T.B. in N. Mochizuki's lab for their assistance. **Funding:** J.V. has
643 received funding from the European Research Council (ERC) under the European
644 Union's Horizon 2020 research and innovation program: H.F. was supported from the
645 University of Strasbourg Institute for Advanced Study (USIAS-2017-097), Takeda
646 Medical Research Foundation, Uehara Memorial Foundation, and Cell Science Research
647 Foundation. **Author contributions:** H.F. and J.V. conceived the project. H.F. designed
648 the work and performed experiments. R.W.C. performed the analysis of Ca^{2+} signaling
649 normalization. H.F., J.X. and N. Minc performed the magnetic tweezer experiments. V.V.
650 and Y.C.H. performed the analysis of 3D simulation. N. Minc and N. Mochizuki provided
651 reagents and suggestions. H.F. and J.V. wrote the manuscript. All authors interpreted the
652 data, contributed to data analysis and discussed the manuscript. **Competing interests:**
653 The authors declare no competing interests. **Data and materials availability:** All images

654 and Tg lines are available in the main text or the supporting materials.

655

656 **Corresponding authors**

657

658 **Materials and Methods:**

659 **Zebrafish (*Danio rerio*) strains, transgenic lines, and mutant lines**

660 The experiments using zebrafish were approved by the animal experimentation
661 committee of the institutional review board of the IGBMC (reference numbers MIN
662 APAFIS#4669–2016032411093030 v4 and MIN 4669–2016032411093030 v4-detail of
663 entry 1) and performed according to the guidelines of the Institute. Embryos were raised
664 in E3 medium and incubated at 28.5°C. Developmental staging was referred to
665 chronological and morphological criteria (68). We used the AB strain as wild-type. The
666 following zebrafish transgenic lines were used for experiments: *Tg(fli1a:gal4ff)* (69),
667 *Tg(uas:GCaMP7a)* (70), *Tg(kdrl:nls-mCherry)^{ncv5}* (71), *Tg(fli1a:lifeact-mCherry)^{ncv7}*
668 (72), *Tg(tp1:d2EGFP)* (73), *Tg(fli1a:myr-mCherry)^{ncv1}* (74), *Tg(fli1a:h2b-mCherry)^{ncv31}*
669 (24), *Tg(myf7:nls-mCherry)^{ncv11}* (75), *Tg(uas:RFP)* (76), and *TgBAC(nfatc1:gal4ff)*
670 (65). The *Tg(4xnfbr:d2EGFP)^{ncv531}*, *TgBAC(twist1b:GFP)^{ncv534}*, *Tg(fli1a:GFP-*
671 *nfatc1)^{ncv532}*, and *Tg(uas:VIVIT-mCherry)^{ncv533}* were generated as described in the
672 experimental procedures. We used FK506, a calcineurin inhibitor, which is blocking
673 valve morphogenesis to test the specificity in the *Tg(fli1a:lifeact-GFP);Tg(kdrl:nls-*
674 *mCherry)* embryos (25, 40) (Fig. S2D). Such treatment significantly suppressed the
675 reporter expression of *Tg(4xnfbr:d2EGFP)* embryos (Fig. S10, A and B). In addition,
676 VIVIT peptide overexpression using a selective inhibitor of Nfat dephosphorylation (77),
677 using the *TgBAC(nfatc1:galff)* driver which is specific to endocardial cells (65) was used.

678 Such treatment also led to the suppression of reporter activation (Fig. S2E), demonstrating
679 that our reporter *Tg(4xnfbr:d2EGFP)* is indeed revealing Nfat activation. The following
680 zebrafish mutants were used for experiments: The knockout alleles of *m651* for *gata1a*
681 (*33*), *ts294e* for *dzip1* (*53*), *tc321* for *trpp2* (*52*), *sa1671* for *trpv4* (*4*) (Zebrafish
682 International Resource Center [ZIRC]), *sa12608* for *piezo1* (European Zebrafish
683 Resource Center [EZRC]), *sa12414* for *piezo2a* (ZIRC), *sa14724* for *piezo2b* (ZIRC).
684 The knockout allele of *ncvxx* for *p2rx1* and *ncvxx* for *p2rx4a* were generated as described
685 in the experimental procedures.

686

687 **Generation of knockout zebrafish by TALEN mutagenesis**

688 To develop knockout zebrafish, we used transcription activator-like effector nuclease
689 (TALEN) Targeter 2.0 (<https://tale-nt.cac.cornell.edu>) to design TALEN pair that targets
690 *p2rx1* and *p2rx4a*. The target sequence of TAL-*p2rx1* and TAL-*p2rx4a* were 5'-
691 TGCCATCGGCTCAGTCTTCACcaagatgaagggagtTCCTTCACTAATATCAGTGGA
692 -3', and 5'-TTCTCAGCTCAGTCACAaccaaagtgaaggAATTGCTTTAACAAACACCA
693 -3', respectively (capital letters were sequences of left [TAL-*p2rx1*-F and TAL-*p2rx4a*-
694 F] and right [TAL-*p2rx1*-R and *p2rx4a*-R] arms, respectively). These expression
695 plasmids of the TALEN-pair were constructed by pT3TS-GoldyTALEN. TALEN
696 mRNAs were synthesized *in vitro* by T3 mMessage mMACHINE kit (Thermo Fisher
697 Scientific). To induce double strand breaks in the target sequence, both 50 pg of TAL-
698 *p2rx1*-F / -*p2rx1*-R mRNAs, and TAL-*p2rx4a*-F / -*p2rx4a*-R mRNAs were injected into
699 1-2-cell stage transgenic embryos, respectively. Each injected founder (F0) fish was
700 outcrossed to wild-type fish to obtain the F1 progeny from individual founders. To
701 analyse TALEN induced mutations, genomic DNA from F1 embryos was lysed by 50 µl

702 of NaOH solution (50 mM) at 95°C for 5 min, and 5 µl of Tris-HCl (pH8.0, 1.0 M) was
703 added on ice for 10 min. After centrifugation (13,500 rpm, 5 min), PCR reaction was
704 performed by KOD FX Neo DNA polymerase (TOYOBO). The genotyping PCR primers
705 were used for amplification: *p2rx1* (5'-GTGTGGAGCCCTGCAATTTTAC-3' and 5'-
706 CAACCCACCTGTTCAGGAAACAC-3', 60°C for annealing); *p2rx4a* (5'-
707 TCATAGCCTACGTTATCGGGTAAG-3' and 5'-
708 CACCAGTGAGTGGTCTGGTCATT-3', 60°C for annealing).

709

710 **Genotyping primers**

711 The following genotyping PCR primers were used for amplification: *piezo1* (5'-
712 CTATTCCTTTGAGAGCCCTTTG-3' and 5'-GCATGTGGATACAGCAATGAC-3',
713 58°C for annealing); *piezo2a* (5'-AATGTGATGTGTTGCTCTGC-3' and 5'-
714 CTTTCAGCAAAGGCATCTCC-3', 60°C for annealing, and for sequence; 5'-
715 TCAGTCTGTTCGGGATTTCTC-3'); *piezo2b* (5'-TGCTAGGTGGTTGGCTTTCTC-3'
716 and 5'-CTTAAAGCTGTGAAGGAGACATC-3', 65°C for annealing, and for sequence;
717 5'-TCTCTGTGGAAGTGTGTTGTG-3'); *gata1a* (5'-
718 GTGAGTATACACAATTACAC-3' and 5'-GGTTCAGAGAATACGCTCCT-3', 53°C
719 for annealing); *trpv4* (5'-GCCTTTCAGCATGTTGTCCA-3' and 5'-
720 GGTTCCTGCTGGTCTACGTG-3', 56°C for annealing); *trpp2* (5'-
721 CCATTAGCCTGCACATTCAATC-3' and 5'-ATCGCACTGCTCATCTGAAG-3',
722 68°C for annealing); *dzip1* (5'-CGGTACAGACACAGCCCAATG-3' and 5'-
723 CGTGAGACCAGTGTAGGTTTC-3', 60°C for annealing, and for sequence; 5'-
724 ACAAACAAATTCAAGTCCAG-3').

725

726 **Image acquisition and definition of the AVC**

727 To clearly obtain images of embryos, a 0.2 mM solution of 1-phenyl-2-thiourea (PTU)
728 (Sigma-Aldrich) was added in breeding E3 media to suppress pigmentation and 0.1
729 mg/mL of MS-222 was added to anesthetize the embryos during embedding. A TCS SP8
730 DLS light sheet confocal microscope (Leica) equipped with 25x water immersion
731 objective (Leica HCX IRAPO L, 0.95 N.A.) and a camera (ORCA-Flash4.0 V2,
732 Hamamatsu) for acquisition. A Lightsheet Z.1 (Zeiss) equipped with 20x water
733 immersion objective (Zeiss, 1.0 N.A.) and two cameras (PCO.edge sCMOS) for
734 simultaneous acquisition. An inverted microscope (Leica, DMi8) combined with a CSU-
735 X1 confocal scanning head (Yokogawa) equipped with a 40x water objective (Leica, 1.1
736 N.A.) and two cameras (ORCA-Flash4.0 V2, Hamamatsu) for simultaneous acquisition.
737 Ca^{2+} influx was visualized by the excitation of the genetically encoded calcium indicator
738 GCaMP7a using a 488 nm wavelength laser line. Excitation of GFP and mCherry was
739 done using 488 nm and 561 nm wavelength laser lines, respectively. Beating heart
740 samples were taken every 10 msec exposure time unless otherwise described and the data
741 were acquired by binning 2 x 2. Confocal images of 1.5 μm steps were taken with an
742 upright TCS SP8 confocal microscope system (Leica) equipped with a 25x water
743 immersion objective (Leica HCX IRAPO L, 0.95 N.A.) and an upright FV3000 confocal
744 microscope system (Olympus) equipped with a 20x water immersion objective (Olympus
745 XLUMPlan FL_N, 1.0 N.A.). Dechorionated embryos were mounted in 1% low-melting
746 agarose (Invitrogen-Thermo Fisher Scientific) dissolved in E3 medium. **At early stages**
747 **(30 hpf and 34 hpf), the pre-AVC region is defined as the middle area between arterial**
748 **pole and venous pole. Furthermore, the tissue curvature is found in the pre-AVC region**
749 **and used as morphological landmarks. After 48 hpf, the endocardial cells on the AVC**

750 region is defined by the area located between the superior and inferior region of the atrium
751 and the ventricular chamber. Images were processed with a Las X software (Leica), Zen
752 3.1 software (Zeiss), FV31S-SW software (Olympus), ImageJ and Imaris 9.6 (Bitplane).

753

754 **Chemical treatments**

755 Embryos were treated with the following small molecule inhibitors: MS-222 (2.0 mg/mL)
756 or BDM (2,3-butanedione monoxime, 30 mM, Sigma-Aldrich) to induce heart arrest; p-
757 amino-blebbistatin (10 μ M, Optopharma), a myosin II inhibitor, to suppress a heartbeat
758 without block the action potential; Gadolinium chloride ($GdCl_3$, 0.2 mM and 1 mM,
759 Sigma-Aldrich), a stretch-activated calcium channel inhibitor, to check the influence of
760 Ca^{2+} influx in EdCs of the AVC; Oligomycin A (50 μ g/mL, Sigma-Aldrich), an inhibitor
761 of mitochondrial ATP synthetase, to reduce the ATP level; 5-BDBD (10 μ M, Sigma-
762 Aldrich), a P2X4 antagonist, to check the function of P2rx4 in the EdCs; NF023 (10 μ M,
763 Tocris), a P2X1 antagonist, to check the function of P2rx1 in the EdCs; A-317491 (10
764 μ M, Sigma-Aldrich), a P2X3 antagonist, to check the function of P2rx3 in the EdCs; A-
765 438079 (10 μ M, Sigma-Aldrich), a P2X7 antagonist, to check the function of P2rx7 in
766 the EdCs; PPADS tetrasodium salt (20 μ M, Tocris), a P2X1, X2, X3 and X5 non-selective
767 antagonist, to check the function of P2X1_2_3_5 in the EdCs; BPTU (25 μ M, Tocris), a
768 P2Y1 antagonist, to check the function of P2Y1 in the EdCs; AR-C118925XX (10 μ M,
769 Tocris), a P2Y2 antagonist, to check the function of P2Y2 in the EdCs; FK506 (2 μ M,
770 Abcam), a calcineurin inhibitor, to validate Nfat reporter activity; Janex-1 (0.4 mM,
771 Abcam), a Jak3 inhibitor, to validate Nfat tyrosine phosphorylation (78); Ki8751 (1 μ M,
772 Tocris), a VEGFR2 inhibitor, to check the effect of Vegfr2 signaling in the EdCs. As a
773 control, the embryos were incubated in E3 solution containing DMSO.

774

775 **Microsurgery to retain the bead into cardiac lumen**

776 Zebrafish embryos were kept ventral side to the top and embedded with 1% low-melting
777 agarose. After mounted, beads (PureCube Glutathione MagBeads, Cube Biotech) were
778 deposited on top of the agarose with E3 medium. A hole was created in the center of the
779 yolk by forceps and the bead of roughly 30-40 μm diameter was inserted into a hole. The
780 bead was pushed anteriorly by the tip of forceps. Once the bead reached the venous pole,
781 suction caused by the heart contraction will move the bead into the cardiac lumen (79).
782 Embryos then were released from agarose and allowed to develop in E3 medium at 28.5°C.
783 Approximately 30% embryos kept the bead move continuously in the atrium or the
784 ventricle together with the blood flow were applied to the experiments. Whereas, the
785 embryos with the bead sucked in the outflow tract were excluded for the experiments.

786

787 **Simulation of influences in the grafted bead in the atrium**

788 A static geometry of the zebrafish atrium was approximated from a 2D fluorescent
789 imaging video of the atrial chamber containing the moving magnetic bead. 2D outlines
790 of the atrial wall and AVC were extracted from the video, imported in ANSYS
791 Workbench 2019 (ANSYS Inc.) and revolved about their respective central axes to
792 generate a 3D shape of the atrial chamber and AVC (Fig. S3A). A 30 μm spherical bead
793 was inserted in the chamber. The atrial chamber was meshed with about 453k tetrahedral
794 cells, and a zone of 30 μm radius from the center of the bead was programmed to have an
795 overset mesh with 384k tetrahedral cells, which were determined by a mesh convergence
796 study. In both meshes, refined mesh at wall boundaries was achieved via 5-10 inflation
797 layers. The overset mesh was superimposed onto the atrial chamber mesh, and together

798 with the bead, was programmed to move with a uni-directional oscillatory motion via
799 ANSYS user-defined function. The bead motion waveform (Fig. S3B) was traced from
800 the 2D video mentioned above. The bead motion was stopped at about 0.44 μm from the
801 atrial wall to avoid numerical problems as an estimation of the impingement. The blood
802 fluid in the atrial chamber was assumed to have a viscosity of 3.5 cP and density of 1060
803 kg/m^3 . The inlet and outlet boundary conditions were set to zero reference pressures. Two
804 cardiac cycle (800 time-steps) was simulated, with results were extracted from the second
805 cycle. In another variant of the simulation, flow velocities were estimated from the inlet
806 boundary via blood cell motions in the video and were imposed as inlet flow boundary
807 conditions to give a more realistic boundary condition, but the results did not vary
808 significant, and this was thus not considered. The limitation of the simulation was that
809 there were no consideration of the motion of the atrial walls, however, given that the bead
810 motion velocity was higher order than atrial wall motion velocity, our simulations'
811 estimate of the peak wall shear stress and pressures at the bead impact location on the
812 atrial wall should still be reasonable reliable.

813

814 **Magnetic tweezer**

815 A magnetic tweezer was used to apply force to magnetic beads (PureCube Glutathione
816 MagBeads, Cube Biotech) (80, 81) grafted into embryos. Embryos were kept on their
817 lateral side and embedded into 1% low-melting agarose and the heartbeat was arrested by
818 addition of BDM or tricaine into E3 medium. The magnetic probe was built from three
819 rod-shaped, strong neodymium magnets (diameter, 4 mm; height, 10 mm; S-04-10-AN;
820 Supermagnet) prolonged by a sharpened steel piece with a tip radius of $\sim 50 \mu\text{m}$ to create
821 a magnetic gradient. The surface of the steel tip was electro-coated with gold to prevent

822 oxidization. The magnetic tweezers were mounted on an inverted epifluorescent
823 microscope (TI-Eclipse, Nikon) combined with a CMOS camera (Hamamatsu), and its
824 position was controlled by a micromanipulator (Injectman 4, Eppendorf). Embryos were
825 filmed with a 20x dry objective (Apo, NA 0.75, Nikon) and a 1.5x magnifier. The
826 microscope was operated with Micro-Manager (Open Imaging). The embryos with the
827 injected beads in the heart were rotated to become aligned with the principal axis of the
828 magnetic tweezer and time-lapse movies were acquired with a time interval of 5 sec. In
829 each experiment, the magnetic force was controlled by the magnet position to shear and/or
830 compress the cells. The positions of the magnet tip and the agarose magbead were
831 recorded in DIC, and the endocardial cells and Ca^{2+} signaling were recorded in
832 fluorescence.

833 The magnetic force was calibrated by first characterizing the large-scale magnetic force
834 field created by the magnet tip. For this, 2.8 μm mono-dispersed magnetic beads were
835 pulled in a viscous test fluid (80% glycerol, viscosity $8.0 \cdot 10^{-2}$ Pa*sec at 22°C) by the
836 magnet to track the beads velocity as a function of the distance to the magnet, yielding:

$$837 \quad V = 195.4 * e^{-\frac{x}{31.3}} + 31.94 * e^{-\frac{x}{84.05}}$$

$$838 \quad V_{300} = 0.9134 \mu\text{m}/\text{s}$$

839 where V is the velocity of the magnetic bead and x is the distance between the bead and
840 the magnet tip. V_{300} is the bead velocity at a distance 300 μm away from the magnet tip.

841 The same experiment performed on agarose magnetic beads with varying sizes at a
842 fixed distance of 300 μm then allowed to compute the net magnetic force, and establish
843 force-size relationships, using the Stokes equation.

844
$$F_{300} = 0.1533 * R^3$$

845 where R is the bead radius (μm). F_{300} is the magnetic force (pN) at a fix distance 300
846 μm from the magnet tip.

847 According to velocity-distance and force-size relationships, we computed the final
848 equation for calculating the magnetic force:

849
$$F = 0.1533 * R^3 * \frac{V_x}{V_{300}}$$

850 where F is the magnetic force (pN), and V_x ($\mu\text{m/s}$) is the velocity at x μm in the
851 magnetic field. Pressure and shear stresses were deduced by projecting the forces,
852 orthogonal or parallel to the tissue plane, respectively, and by dividing them a measured
853 contact surface area between the bead and the tissue.

854

855 **Microinjection into cardiac lumen**

856 *Tg(fli1a:galff);Tg(uas:GCaMP7a);Tg(kdrl:nls-mCherry)* embryos were kept lateral side
857 and embedded into 1% low-melting agarose. After mounted, we injected with 2 nL of
858 apyrase (0.9 U/ μL , Sigma-Aldrich), ATP γ S tetralithium salt (45 mM, Tocris), and
859 Oligomycin A (25 $\mu\text{g/mL}$) together with red fluorescent 0.5 μm Fluospheres (Thermo
860 Fisher Scientific) using Nanoject II (Drummond) into the region of common cardinal vein.
861 To confirm the precise injection, circulation of Fluospheres in cardiac lumen was checked
862 by the fluorescent stereo zoom microscope (Leica MZ FLIII), and a lightsheet microscope
863 was used to evaluate the Ca^{2+} influx.

864

865 **Microinjection of MOs, mRNAs and Tol2 plasmids**

866 We injected 1 nL of the following Morpholino oligonucleotides (MOs, Gene Tools): 0.5
867 mM of *gata1a* atg-MO (5'-CTGCAAGTGTAGTATTGAAGATGTC-3') (34); 0.15 mM
868 of *tnnt2a* atg-MO (5'-CATGTTTGCTCTGATCTGACACGCA-3') (82); 0.6 mM of
869 *control* MO (5'-CCTCTTACCTCAGTTACAATTTATA-3'); 0.6 mM of *trpp2* atg-MO
870 (5'-AGGACGAACGCGACTGGAGCTCATC-3') (83); 0.6 mM of *kif3a* atg-MO (5'-
871 GTCCAGCTTATTGCTCGGCATTATC-3') (84); 0.35 mM of *myh6* atg-MO (5'-
872 ACTCTGCCATTAAAGCATCACCCAT-3') (85); 0.3 mM of *p2rx4a* splice-MO (5'-
873 AAATGCTGAGCCATAACCATCTCCAC-3'). To check the *p2rx4a* MO efficiency, we
874 used following primers; 5'-TCGTGCTGACCAACATGATCATCAC-3' and 5'-
875 TTCGGGGGATCGACAATTTTTTCT-3'. MOs, mRNAs, and Tol2 plasmids were
876 injected into blastomeres using Nanoject II (Drummond) and IM300 Microinjector
877 (Narishige) at one- to two-cell stage.

878

879 **Plasmids**

880 cDNA fragments encoding zebrafish Klf2a, Klf4a, Egr1, Notch1b, P2rx1, P2rx4a and
881 P2rx7 were amplified by PCR using Phusion high-fidelity PCR master mix (Thermo
882 Fisher Scientific) and a cDNAs library derived from zebrafish embryos, and subcloned
883 into pCR4 Blunt TOPO vector (Thermo Fisher Scientific). The following primers set
884 were used for amplification: *klf2a* (5'-
885 aactcgagAAGGATGAACTGGACAGGTCCATG-3' [containing XhoI sequence] and
886 5'-CTGTGATGAGCCTTCAAGTGAGAAC-3'); *klf4a* (5'-
887 aactcgagGAGCTGGAGCTGCTGGACTATGACT-3' [containing XhoI sequence] and
888 5'-CGCTGTCAGCGTTGGTATTATATC-3'); *egr1* (5'-

889 aactcgagAGCAGTTTGATCACCTTGCTGGAG-3' [containing XhoI sequence] and 5'-
 890 TTCTGTCCTGTGTGGATGCGGATG-3'); *p2rx1* (5'-
 891 aagctagcGGTGTTTCATGTATGAGAAAGGCTACC-3' [containing NheI sequence] and
 892 5'-CGCTGTCAGCGTTGGTATTATATC-3'); *p2rx4a* (5'-
 893 aagctagcGTGTGTCTACAACAAAGGCTACCAAG-3' [containing NheI sequence] and
 894 5'-CAATCCAGTCACAGATGACGTTTAC-3'); *p2rx7* (5'-
 895 aagctagcACCTGCTCTTTTGGCTGCAGCAGAAA-3' [containing NheI sequence] and
 896 5'-GACGAAGACTGTATGGTCTCCAGTA-3').

897 The cDNA of humanP2X4 and zebrafishP2rX4a are cloned into pmCherry-N1 vector and
 898 mutated C353W and C365W, respectively. The following primers were used for cloning:
 899 NheI-hP2X4WT-S (5'-aaGCTAGCccATGgcgggctgctgcgccgc-3') and AgeI-hP2X4WT-
 900 AS (5'-atACCGGTtgtgtgctccagctcactagcaaga-3'); hP2X4C353W-S (5'-
 901 gtgctgTGGgacatcatagtctctac-3') and hP2X4C353W-AS (5'-
 902 gatgtcCCAcagcagcggtcgccatgcc-3'); NheI-zP2rx4aWT-S (5'-
 903 caGCTAGCgttcacaATGagtgaaagtgttg-3') and AgeI-zP2rx4aWT-AS (5'-
 904 atACCGGTtgtttgtcttcgtgtgtaaaagtccg-3'); zP2rx4aC365W-S (5'-
 905 gtcacTGGgactggattgtgttgaca-3') and zP2rx4aC365W-AS (5'-
 906 ccagtcCCAgatgacgttcaccaggcct-3'). These cDNAs (hP2X4WT, hP2X4C353W,
 907 zP2rx4aWT and zP2rx4aC365W) were subcloned into the pCS2 vector (Clontech) and
 908 synthesized capped mRNAs using mMESSAGING mMACHINE T7 transcription kit
 909 (Thermo Fisher Scientific). The embryos were injected 125 pg of each mRNAs into
 910 blastomeres at one- to two-cell stage. All these cDNAs and mutations were confirmed by
 911 DNA sequencing.

912

913 **Generation of transgenic lines**

914 To monitor the nfat signal activation, we established a transgenic reporter zebrafish line
915 expressing destabilized EGFP (d2EGFP) under the control of four times Nfat binding
916 element tandem sequence repeats (4xnfbr)-dependent E1b minimal promoter activation;
917 *Tg(4xnfbr:d2EGFP)^{ncv531}*. The primers based on 1xNfbr sequence (77) attached with
918 flanking XhoI (G/TCGAC) and SalI (C/TCGAG) site (XhoI-1xNfbr-SalI-S, 5'-
919 TCGAGacgccttctgtatgaaacagttttccaggG-3'; XhoI-1xNfbr-SalI-AS, 5'-
920 TCGACcctggaaaaactgtttcatacagaaggcgtC-3'; small letters represent 1x nfat binding
921 element) were ligated together to make a single linear DNA fragment and digested the
922 products with XhoI and SalI to eliminate the inverted repeats as these DNAs contain
923 reconstituted XhoI and SalI sites. DNA fragments were applied agarose gel
924 electrophoresis and collected a fragment around the 150 bp as a 4x tandem oligomers. A
925 4xnfbr tandem oligomers were ligated into both XhoI and SalI-digested pTol2 fragment
926 to make a pTol2-4xnfbr vector. The sequence of 4x tandem repeats was confirmed by
927 DNA sequence. pTol2-4xnfbr vector was inserted with E1b minimal promoter and
928 d2EGFP-polyA sequence to construct the pTol2-4xNfbr-E1b-d2EGFP-pA plasmid.

929 To monitor the nfat signal inhibition, we established a transgenic line expressing VIVIT-
930 mCherry under the control of Gal4-UAS system; *Tg(uas:VIVIT-mCherry)^{ncv533}*. We used
931 a pmCherry-N1 vector as a template and VIVIT peptide (MAGPHPVIVITGPHEE) oligo
932 sequence is inserted upstream of mCherry site by inverse PCR using the following
933 primers: VIVIT-mCherry-S; 5'-
934 atggcgggaccacaccagtaatcgtaattaccggccacacgaggagggccccctgtcgctagcATGGTGAGC
935 AAGGGCGAGGAGGATAAC-3' and VIVIT-mCherry-AS; 5'-
936 GGTGGCGACCGGTGGATCCCGGGCCCGCGGTAC-3' to make VIVIT-mCherry-

937 pA plasmid. The fragment of VIVIT-mCherry-pA site is inserted into pTol2-crystallin-
938 Nls-mCherry-5xuas vector to establish the pTol2-crystallin-Nls-mCherry-5xuas-VIVIT-
939 mCherry-pA plasmid.

940 To monitor the EndoMT, we established a GFP reporter transgenic line under the
941 control of *twist1b* BAC enhancer/promoter; *TgBAC(twist1b:GFP)^{nev534}*. pRedET
942 plasmid (Gene Bridges, Heidelberg, Germany) was introduced into E. coli containing
943 CH73-181M7 BAC clone encoding *twist1b* gene (BacPAC resources) by
944 electroporation (1800V, 25 mF, 200 Ω). Tol2 long terminal repeats in opposite
945 directions flanking ampicillin resistance cassette were amplified by PCR using
946 Tol2_amp as a template and were inserted into the BAC vector backbone. The cDNA
947 encoding GFP together with a kanamycin resistance cassette (GFP_KanR) was
948 amplified by PCR using pCS2-GFP_KanR plasmid as a template and inserted into the
949 start ATG of the *twist1b* gene. Primers to amplify the GFP_KanR for *twist1b* were 5'-
950 atgctggaataacgtccttattcgcacgcgcttcagcagagacttaagcACCATGGTGAGCAAGGGCGAG
951 GAG-3' and 5'-
952 tccgcgggagacacgggggagctggaggagtctcgcggggctcttcgggTCAGAAGAAGCTCGTCAAG
953 AAGGCG-3' (small letters; homology arm to BAC vector, and capital letters; primer
954 binding site to the template plasmid).

955 To monitor the subcellular localization of Nfatc1 in the EdCs, we established a transgenic
956 line expressing GFP-tagged Nfatc1 under the control of *flila* promoter; *Tg(flila:GFP-*
957 *Nfatc1)^{nev532}*. Primers to amplify the human-Nfatc1 (hNfatc1) were (5'-
958 agatctCCAAGCACCAGCTTTCCAGTCCCTTC-3' [containing BglII sequence] and 5'-
959 gtcgacCAGTTAAATGTGCAACACGCCAC-3' [containing SalI sequence]). The
960 construct was inserted into the pEGFP-C1 vector to establish pEGFP-hNfatc1. The

961 EGFP-hNfatc1 was inserted into pTol2-fli1epEGFP-DEST (Addgene #73491) backbone
962 vector to establish the pTol2-fli1a promoter-GFP-Nfatc1.
963 Tol2-mediated zebrafish transgenesis was performed by injecting 30 pg of transgene
964 plasmid together with 50 pg of *tol2 transposase* mRNA, followed by subsequent
965 screening of F1 founders and establishment of stable transgenic strains through selection
966 in F3 generations.

967

968 **Ca²⁺ influx normalisation**

969 To monitor the Ca²⁺ signal during heart development, we crossed the
970 *Tg(fli1a:gal4ff);Tg(uas:GCaMP7a)* line, where a fluorescent Ca²⁺ sensor protein
971 GCaMP7a is driven by endocardial gal4, with the *Tg(kdrl:nls-mCherry)* line, where kdrl-
972 promoter drives nls-mCherry and thus labels endocardial nuclei. To measure the
973 normalised calcium signal of a particular cell over time, we developed software in Matlab
974 (Mathworks) to do the following: For each embryo, the cells imaged move in and out of
975 the focus plane during heartbeat, causing fluctuations in the detectable calcium signal.
976 Our first step was thus to transform our XYT movies into XYtR movies, where T is the
977 timepoints acquired, t is the timepoint along the cardiac cycle, and R is the iteration of
978 cardiac cycles. To do so, we must account for the changes in heartrate over the period of
979 imaging. Using Matlab, we selected nine region of interests (ROIs) one tenth of the size
980 of the whole image and measured the fluorescence intensity of the nuclear channel over
981 time, $I_{\text{nuclear}}(T)$. We calculate the position of the intensity peaks based using `ct_getpeaks`
982 (86) and select two ROIs where the fluctuations in nuclear channel intensity due to
983 heartbeat are the clearest. Next, we averaged the peak positions acquired from the two
984 ROIs iteratively. Each of these averaged peak positions are assumed to correlate to a

985 specific position within the cardiac cycle. We then calculated the average number of
986 timepoints between these peaks to get the average period of heartbeat t_{\max} . We cut the
987 XYT movie into sections with length of $(t_{\max} + 7 \text{ images})$; each centered around the image
988 corresponding to the averaged peak position. We then recombined the sections into a
989 XYtR movie.

990 For each cell of interest within the embryo, we created XYR movie: The XYtR movie is
991 opened in FIJI, the timepoint along the cardiac cycle that best captures the cell of
992 interest was manually identified, and an XYR movie was created for that timepoint.

993 *Image of average signal:* Importing the XYR movie back into Matlab, an image that
994 showed the average calcium and average nuclear signal over the entire course of
995 imaging was calculated. For both channels, each pixel in the final image is the sum of
996 the signal intensity divided over the total number of images, R_{\max} . *Normalised calcium*
997 *signal:* Using the image of the average signal as a guide, we manually drew around the
998 cell of interest to generate the ROI. The normalised calcium signal for the ROI was then
999 calculated using: where I_{calcium} is the fluorescence intensity of the calcium signal, I_{nuclear}
1000 is the fluorescence intensity of the nuclear signal, and the baseline is the minimum
1001 $I_{\text{calcium}}/I_{\text{nuclear}}$ over the entire XYR movie. *Calculate peak position:* The position of the
1002 peaks was calculated using `ct_pulseanalysis` (86) with the SMOOTH parameter set to 5.

1003

1004 **Whole-mount in situ hybridization (WISH)**

1005 The antisense *klf2a*, *klf4a*, *egr1*, *p2rx1*, *p2rx4a* and *p2rx7* RNA probes labeled with
1006 digoxigenin (DIG) were prepared by using an RNA labeling kit (Roche). WISH was
1007 performed as previously described (87). Colorimetric reaction was carried out using BM
1008 purple (Roche) as the substrate. To stop the reaction, embryos were washed with PBS-T,

1009 fixed with 4% PFA for 20 min at room temperature and subsequently immersed in
1010 glycerol. Images were taken using a stereo microscope (Leica M165C).

1011

1012 **RNAscope analysis**

1013 Embryos were fixed by 10% NBF for overnight at room temperature. After fixation, the
1014 solution was changed to 50% Methanol / PBBT (PBS with 2 mg/mL BSA and 0.1%
1015 TritonX-100) for 10 min, then changed to 100% Methanol at room temperature, and then
1016 stored in 100% Methanol at -20°C overnight. After rehydration, embryos were washed
1017 three-times for 10 min in PBBT. Embryos were treated in PBBT with protease plus for
1018 30 min at room temperature, and subsequently washed three-times for 10 min in PBBT.
1019 For the probe hybridization, embryos were treated in the following probe mixture
1020 (ACDbio): *kdrl*-C1 probe with *p2rx1*-C3, *p2rx4a*-C3 or *p2rx7*-C3 probes; *klf4a*-C1 probe
1021 with *klf2a*-C2 probe; *wnt9b*-C1 probe with *klf2a*-C2 probe; *kdrl*-C1 probe with *gata1a*-
1022 C3 probe for overnight at 40°C. Embryos were washed and amplified the hybridization
1023 following the workflow in ACDbio. Embryos were and stored in PBBT at 4°C prior to
1024 confocal imaging.

1025

1026 **Data analysis**

1027 Data was analyzed using GraphPad Prism 7 (GraphPad Software). All columns are
1028 indicated as mean \pm s.d. Statistical significance of multiple groups was determined by
1029 one-way ANOVA with Tukey's tests. Statistical significance among two groups was
1030 determined by Student's t-test with a two-tailed distribution. Data were considered
1031 statistically significant if the p-value <0.05 (*), <0.01 (**), <0.0001 (****).

1032

1033

Reference List

1034

1035

1036 1. T. Iskratsch, H. Wolfenson, M. P. Sheetz, *Nat. Rev. Mol. Cell Biol.* **15**, 825-833
1037 (2014).

1038 2. T. Mammoto, A. Mammoto, D. E. Ingber, *Annu. Rev. Cell Dev. Biol.* **29**, 27-61
1039 (2013).

1040 3. D. J. Beech, A. C. Kalli, *Arterioscler. Thromb. Vasc. Biol.* **39**, 2228-2239 (2019).

1041 4. E. Heckel *et al.*, *Curr. Biol.* **25**, 1354-1361 (2015).

1042 5. S. S. Ranade *et al.*, *Proc. Natl. Acad. Sci. U. S. A* **111**, 10347-10352 (2014).

1043 6. J. Xu *et al.*, *Cell* **173**, 762-775 (2018).

1044 7. J. I. Hoffman, S. Kaplan, *J. Am. Coll. Cardiol.* **39**, 1890-1900 (2002).

1045 8. C. Dina *et al.*, *Nat. Genet.* **47**, 1206-1211 (2015).

1046 9. R. Durst *et al.*, *Nature* **525**, 109-113 (2015).

1047 10. V. Garg *et al.*, *Nature* **437**, 270-274 (2005).

1048 11. A. A. Richards, V. Garg, *Curr. Cardiol. Rev.* **6**, 91-97 (2010).

1049 12. M. P. White *et al.*, *J. Mol. Cell Cardiol.* **84**, 13-23 (2015).

1050 13. R. A. Levine *et al.*, *Nat. Rev. Cardiol.* **12**, 689-710 (2015).

1051 14. N. Baeyens, C. Bandyopadhyay, B. G. Coon, S. Yun, M. A. Schwartz, *J. Clin.*
1052 *Invest* **126**, 821-828 (2016).

1053 15. M. A. Schwartz, D. Vestweber, M. Simons, *Science* **360**, 270-271 (2018).

1054 16. K. Yamamoto *et al.*, *J. Cell Sci.* **124**, 3477-3483 (2011).

1055 17. R. M. Davidson, D. W. Tatakis, A. L. Auerbach, *Pflugers Arch.* **416**, 646-651
1056 (1990).

1057 18. J. B. Lansman, T. J. Hallam, T. J. Rink, *Nature* **325**, 811-813 (1987).

- 1058 19. C. Wei *et al.*, *Nature* **457**, 901-905 (2009).
- 1059 20. S. Xu, A. D. Chisholm, *Curr. Biol.* **21**, 1960-1967 (2011).
- 1060 21. W. S. Beane, J. Morokuma, D. S. Adams, M. Levin, *Chem. Biol.* **18**, 77-89 (2011).
- 1061 22. M. Levin, C. G. Stevenson, *Annu. Rev. Biomed. Eng* **14**, 295-323 (2012).
- 1062 23. J. G. Goetz *et al.*, *Cell Rep.* **6**, 799-808 (2014).
- 1063 24. Y. Yokota *et al.*, *Elife.* **4**, (2015).
- 1064 25. C. P. Chang *et al.*, *Cell* **118**, 649-663 (2004).
- 1065 26. F. Gunawan, A. Gentile, S. Gauvrit, D. Stainier, A. Bensimon-Brito, *Circ. Res.*
1066 (2020).
- 1067 27. A. M. Ranger *et al.*, *Nature* **392**, 186-190 (1998).
- 1068 28. B. Zhou *et al.*, *Development* **132**, 1137-1146 (2005).
- 1069 29. R. A. Schulz, K. E. Yutzey, *Dev. Biol.* **266**, 1-16 (2004).
- 1070 30. B. Wu, H. S. Baldwin, B. Zhou, *Trends Cardiovasc. Med.* **23**, 294-300 (2013).
- 1071 31. W. M. Flanagan, B. Corthesy, R. J. Bram, G. R. Crabtree, *Nature* **352**, 803-807
1072 (1991).
- 1073 32. J. L. Galloway, R. A. Wingert, C. Thisse, B. Thisse, L. I. Zon, *Dev. Cell* **8**, 109-
1074 116 (2005).
- 1075 33. S. E. Lyons *et al.*, *Proc. Natl. Acad. Sci. U. S. A* **99**, 5454-5459 (2002).
- 1076 34. J. Vermot *et al.*, *PLoS. Biol.* **7**, e1000246 (2009).
- 1077 35. F. Boselli, E. Steed, J. B. Freund, J. Vermot, *Development* **144**, 4322-4327 (2017).
- 1078 36. J. B. Freund, J. Vermot, *Biophys. J.* **106**, 752-762 (2014).
- 1079 37. T. Bartman *et al.*, *PLoS. Biol.* **2**, E129 (2004).
- 1080 38. Y. Y. Foo *et al.*, *Biomech. Model. Mechanobiol.* **19**, 221-232 (2020).

- 1081 39. F. Boselli, J. Vermot, *Methods* **94**, 129-134 (2016).
- 1082 40. D. Beis *et al.*, *Development* **132**, 4193-4204 (2005).
- 1083 41. G. Luxan, G. D'Amato, D. MacGrogan, J. L. de la Pompa, *Circ. Res.* **118**, e1-e18
1084 (2016).
- 1085 42. L. A. Timmerman *et al.*, *Genes Dev.* **18**, 99-115 (2004).
- 1086 43. J. L. de la Pompa *et al.*, *Nature* **392**, 182-186 (1998).
- 1087 44. E. Steed *et al.*, *Nat. Commun.* **7**, 11646 (2016).
- 1088 45. L. M. Goddard *et al.*, *Dev. Cell* **43**, 274-289 (2017).
- 1089 46. B. Lai *et al.*, *Am. J. Physiol Heart Circ. Physiol* **315**, H1293-H1303 (2018).
- 1090 47. A. D. Egorova *et al.*, *Circ. Res.* **108**, 1093-1101 (2011).
- 1091 48. T. Banjo *et al.*, *Nat. Commun.* **4**, 1978 (2013).
- 1092 49. R. Ferreira, H. Fukui, R. Chow, A. Vilfan, J. Vermot, *J. Cell Sci.* **132**, (2019).
- 1093 50. A. L. Duchemin, H. Vignes, J. Vermot, R. Chow, *Curr. Opin. Genet. Dev.* **57**,
1094 106-116 (2019).
- 1095 51. A. L. Duchemin, H. Vignes, J. Vermot, *Elife.* **8**, (2019).
- 1096 52. J. Schottenfeld, J. Sullivan-Brown, R. D. Burdine, *Development* **134**, 1605-1615
1097 (2007).
- 1098 53. K. Sekimizu *et al.*, *Development* **131**, 2521-2532 (2004).
- 1099 54. P. Campinho, P. Lamperti, F. Boselli, A. Vilfan, J. Vermot, *Cell Rep.* **31**, 107505
1100 (2020).
- 1101 55. K. Yamamoto, R. Korenaga, A. Kamiya, J. Ando, *Circ. Res.* **87**, 385-391 (2000).
- 1102 56. K. Yamamoto, H. Imamura, J. Ando, *Am. J. Physiol Heart Circ. Physiol* **315**,
1103 H1477-H1485 (2018).
- 1104 57. J. P. Green *et al.*, *Cardiovasc. Res.* **114**, 324-335 (2018).

- 1105 58. R. A. North, *Physiol Rev.* **82**, 1013-1067 (2002).
- 1106 59. A. L. Armesilla *et al.*, *Mol. Cell Biol.* **19**, 2032-2043 (1999).
- 1107 60. C. P. Heisenberg, Y. Bellaïche, *Cell* **153**, 948-962 (2013).
- 1108 61. T. Mammoto, D. E. Ingber, *Development* **137**, 1407-1420 (2010).
- 1109 62. T. Merle, E. Farge, *Curr. Opin. Cell Biol.* **55**, 111-118 (2018).
- 1110 63. S. Donat *et al.*, *Elife.* **7**, (2018).
- 1111 64. F. Gunawan *et al.*, *J. Cell Biol.* **218**, 1039-1054 (2019).
- 1112 65. J. Pestel *et al.*, *Development* **143**, 2217-2227 (2016).
- 1113 66. J. Li *et al.*, *Nature* **515**, 279-282 (2014).
- 1114 67. K. Nonomura *et al.*, *Proc. Natl. Acad. Sci. U. S. A* **115**, 12817-12822 (2018).
- 1115 68. C. B. Kimmel, W. W. Ballard, S. R. Kimmel, B. Ullmann, T. F. Schilling, *Dev.*
1116 *Dyn.* **203**, 253-310 (1995).
- 1117 69. L. Herwig *et al.*, *Curr. Biol.* **21**, 1942-1948 (2011).
- 1118 70. A. Muto, M. Ohkura, G. Abe, J. Nakai, K. Kawakami, *Curr. Biol.* **23**, 307-311
1119 (2013).
- 1120 71. Y. Wang *et al.*, *Development* **137**, 3119-3128 (2010).
- 1121 72. Y. Wakayama, S. Fukuhara, K. Ando, M. Matsuda, N. Mochizuki, *Dev. Cell* **32**,
1122 109-122 (2015).
- 1123 73. B. S. Clark *et al.*, *Development* **139**, 1599-1610 (2012).
- 1124 74. S. Fukuhara *et al.*, *Dev. Biol.* **393**, 10-23 (2014).
- 1125 75. H. Fukui *et al.*, *Dev. Cell* **31**, 128-136 (2014).
- 1126 76. K. Asakawa *et al.*, *Proc. Natl. Acad. Sci. U. S. A* **105**, 1255-1260 (2008).
- 1127 77. J. Aramburu *et al.*, *Science* **285**, 2129-2133 (1999).

- 1128 78. A. K. Patra *et al.*, *Nat. Immunol.* **14**, 127-135 (2013).
- 1129 79. J. R. Hove *et al.*, *Nature* **421**, 172-177 (2003).
- 1130 80. J. Salle *et al.*, *J. Cell Biol.* **218**, 771-782 (2019).
- 1131 81. H. Tanimoto, J. Salle, L. Dodin, N. Minc, *Nat. Phys.* **14**, 848-854 (2018).
- 1132 82. S. Korzh *et al.*, *BMC. Dev. Biol.* **8**, 84 (2008).
- 1133 83. Z. Sun *et al.*, *Development* **131**, 4085-4093 (2004).
- 1134 84. Z. Liu *et al.*, *Nat. Commun.* **10**, 1839 (2019).
- 1135 85. E. Berdougo, H. Coleman, D. H. Lee, D. Y. Stainier, D. Yelon, *Development* **130**,
1136 6121-6129 (2003).
- 1137 86. Y. P. Hung *et al.*, *Elife.* **6**, (2017).
- 1138 87. H. Fukui *et al.*, *Elife.* **7**, (2018).
- 1139
- 1140